

AD-A281 936



ATION PAGE

Form Approved
OMB No. 0704-0188

to average 1 hour per response, including the time for reviewing instructions, searching existing data sources, gathering the collection of information. Send comments regarding this burden estimate or any other aspect of this form to Washington Headquarters Services, Directorate for Information Operations and Reports, 1215 Jefferson Avenue, Washington, DC 20540.

1. AGENCY USE ONLY (Leave blank)		2. REPORT DATE 31 May 94	3. REPORT TYPE AND DATES COVERED Final: 1 May 91 to 31 Jan 94	
4. TITLE AND SUBTITLE Capacitance Calculations in Nanostructure Devices via the Quantum Liouville Equation in the Coordinate Representation			5. FUNDING NUMBERS DAAL03-91-C-0035	
6. AUTHOR(S) Harold L. Grubin and T.R. Govindan			94-21294 	
7. PERFORMING ORGANIZATION NAME(S) AND ADDRESS(ES) Scientific Research Associates, Inc. 50 Nye Road, P.O. Box 1058 Glastonbury, CT 06033-6058				
9. SPONSORING/MONITORING AGENCY NAME(S) AND ADDRESS(ES) U.S. Army Research Office P.O. Box 12211 Research Triangle Park, NC 27709-2211			10. SPONSORING/MONITORING AGENCY REPORT NUMBER AR0.28646.4-EL	
11. SUPPLEMENTARY NOTES The views, opinions and/or findings contained in this report are those of the author(s) and should not be construed as an official Department of the Army position, policy, or decision, unless so designated by other documentation.				
12a. DISTRIBUTION/AVAILABILITY STATEMENT Approved for public release; distribution unlimited.			12b. DISTRIBUTION CODE	
13. ABSTRACT (Maximum 200 words) Through the use of numerical methods the quantum Liouville equation in the coordinate representation has been implemented for the study of semiconductor devices with nanoscale feature sizes. This document summarizes work performed under US Army Contract DAAL03-91-C-0035 to evaluate the significance of calculating the capacitance voltage characteristics of quantum structures via the quantum Liouville equation. All studies were to be performed with a user-friendly workstation based algorithm, copies of which have been placed at the U.S. Army Research Laboratory at Fort Monmouth.				
14. SUBJECT TERMS Capacitance-voltage, quantum transport, Liouville equation, gallium arsenide, workstation-menu, dissipation, nanostructures			15. NUMBER OF PAGES 49	
17. SECURITY CLASSIFICATION OF REPORT UNCLASSIFIED			16. PRICE CODE	
18. SECURITY CLASSIFICATION OF THIS PAGE UNCLASSIFIED		19. SECURITY CLASSIFICATION OF ABSTRACT UNCLASSIFIED		20. LIMITATION OF ABSTRACT UL

94 7 12 001

Scientific Research Associates, inc.

50 Nye Road, P.O. Box 1058
Tel: (203) 659-0333

Glastonbury, Connecticut 06033
Fax: (203) 633-0676

FINAL REPORT R-9332F

CAPACITANCE CALCULATIONS IN NANOSTRUCTURE DEVICES VIA THE QUANTUM LIOUVILLE EQUATION IN THE COORDINATE REPRESENTATION

by
Harold L. Grubin and T.R Govindan

Contract DAAL03-91-C-0035

**Submitted to
Department of the Army
U.S. Army Research Office
P. O. Box 12211
4300 South Miami Blvd.
Research Triangle Park, NC 27709-2211**

May 1994

**Approved for Public Release;
Distribution Unlimited**

Accession For		
NTIS	CRA&I	<input checked="" type="checkbox"/>
DTIC	TAB	<input type="checkbox"/>
Unannounced		<input type="checkbox"/>
Justification		
By		
Distribution /		
Availability Codes		
Dist	Avail and/or Special	
A-1		

CAPACITANCE CALCULATIONS IN NANOSTRUCTURE DEVICES VIA THE QUANTUM LIOUVILLE EQUATION IN THE COORDINATE REPRESENTATION

TABLE OF CONTENTS

ABSTRACT	i
1. INTRODUCTION	1
1.1 Background.....	1
1.2 General Comments.....	2
1.3 Comments Specific to the Capacitance Studies.....	3
1.4 Comments on SRA's Publications.....	3
2 CAPACITANCE-VOLTAGE CALCULATIONS	4
2.1 Introduction.....	4
2.2 Low/High/Intermediate Uniform N_0 Heterostructure.....	6
2.3 Double Barrier Uniform N_0	12
2.4 Staggered Heterostructure Uniform N_0	16
2.5 Single Barrier, Nonuniform N_0	21
3. DISSIPATION CALCULATIONS-.....	24
3.1 Introduction to the Phenomenological Model.....	24
3.2 The Phenomenological Model: Single barrier, constant scattering time.....	25
4. ETIOLOGY OF THE PHENOMENOLOGICAL DISSIPATION MODEL	29
4.1 The Quantum Liouville Equation	29

4.2 Phenomenological Scattering Potentials and Quasi-Fermi Levels.....	32
4.3 Consistency with the Quantum Hydrodynamic Equations	34
5. GENERALIZED SCHOTTKY BARRIERS FOR CV STUDIES.....	35
5.1 Introduction.....	35
5.2 The Schottky Barrier Model	35
5.3 The Schottky Barrier as an Interface Model / Quasi Fermi Levels	41
6. SUMMARY	45

CAPACITANCE CALCULATIONS IN NANOSTRUCTURE DEVICES VIA THE QUANTUM LIOUVILLE EQUATION IN THE COORDINATE REPRESENTATION

ABSTRACT

Through the use of numerical methods the quantum Liouville equation in the coordinate representation has been implemented for the study of semiconductor devices with nanoscale feature sizes. This document summarizes work performed under US Army Contract DAAL03-91-C-0035 to evaluate the significance of calculating the capacitance voltage characteristics of quantum structures via the quantum Liouville equation. All studies were to be performed with a user-friendly workstation based algorithm, copies of which have been placed at the U.S. Army Research Laboratory at Fort Monmouth.

CAPACITANCE CALCULATIONS IN NANOSTRUCTURE DEVICES VIA THE QUANTUM LIOUVILLE EQUATION IN THE COORDINATE REPRESENTATION

1. INTRODUCTION

1.1 Background

Differential capacitance versus voltage (C - V) measurements permit a reconstruction of density profiles in semiconductor heterostructures based upon a standard textbook formula:

$$(1) \quad N_{reconstructed}(< x >) \propto \left[\frac{dC^{-2}}{dV} \right]^{-1},$$

where:

$$(2) \quad C = \frac{\epsilon}{< x >}$$

and $< x >$, which is implicitly defined in terms of a measured or computed capacitance is *extremely* sensitive to changes in applied bias. As we will see, equation (1) provides an excellent measure of the charge distribution of nanoscale elements. Further, the extrapolated intercept of $1/C^2$ versus V yields the offset voltage for simple heterostructure configurations. Thus from a single set of measurements qualitative information regarding the position of the key heterointerfaces, and quantitative information concerning the offset voltages are obtained. *This study was devoted to determining the significance of this method for reliably analyzing the profiles of mesoscopic structures.*

For the past decade CV studies have included a numerical component involving the solution of Poisson's equation for a density distribution computed either from the drift and diffusion equations or Schrodinger's equation (coupled to the equilibrium Fermi-Dirac distribution). The numerical component was implemented for specific heterostructure configurations, from which *computed CV characteristics are obtained*. The theoretical structure providing the closest fit

between the calculated and measured CV relation and consequent reconstructed density was often pronounced as the one representing the actual heterostructure.

The degree to which theory is a reliable guide to CV measurements is dependent upon:

- (a) the fundamental equations chosen to represent the structure (quantum structures require equations describing quantum transport);
- (b) the statistics, either Boltzmann or Fermi statistics;
- (c) traps and unusual doping contributions (e.g. planar doping)
- (d) the ability to treat nonequilibrium conditions in which the distribution functions represents quantum effects;
- (e) the ability to treat specific quantum boundary effects.

In short the most representative calculation is that with the most physics. Thus, the equations least likely to offer confidence in the reconstructed calculations are based upon classical equations, e.g., the drift and diffusion equations. The equations most likely to offer confidence are those yielding quantum distribution functions, such as the Wigner function or the density matrix.

Under ARO Contract DAAL03-91-C-0035 Scientific Research Associates, Inc. (SRA) has solved and applied the equation of motion of the density matrix in the coordinate representation to examining capacitive effects in quantum structures. This document summarizes these studies.

1.2 General Comments

1. SRA's density matrix algorithm has been used to solve the Liouville equation in the coordinate representation for electrons and holes in semiconductor with heterostructures, barriers and wells. The code, originally implemented for CRAY computers, has been reconfigured for work station computation. Presently, all quantum studies with the density matrix are performed on work stations.

2. A menu-driven point-and-click work-station version of SRA's density matrix algorithm, named DENMAT (density matrix) has been used by the Principle Investigator for all of the calculations in the study.

3. A copy of DENMAT has been placed at the Army Research Laboratory at Fort Monmouth. R. Lux is evaluating DENMAT.

1.3 Comments Specific to the Capacitance Studies

4. Quantum distribution calculations are necessary for the correct evaluation of density, self-consistent potential energy and the intersection of the capacitance voltage curve and the bias axis. The latter provides key device parameters and is a function of temperature and density.

5. The code is being prepared for routine use as an adjunct to experiment.

1.4 Comments on SRA's Publications

6. A major paper discussing the structure of the equations and the results to be obtained using DENMAT has been published; four additional papers have either been published or have been accepted for publication.

7. An invited paper has been presented at the *Computational Electronics Conference* (Leeds, England), and an invited book chapter in *Solid State Physics*, Academic Press, has been written.

Copies of the above papers are incorporated into this final report.

2 CAPACITANCE-VOLTAGE CALCULATIONS

2.1 Introduction

The CV calculation is illustrated for several heterostructure configurations. Standard formulae were used to evaluate the capacitance, with density distributions obtained from the quantum Liouville equation in the coordinate representation. The quantum Liouville equation in the coordinate representation is discussed in a later chapter. While the capacitance is obtained under zero current conditions, the algorithm was generalized to include current and dissipation in anticipation of additional studies in which the capacitance as obtained under finite current conditions. Several calculations with current flow illustrate.

Calculations were either for a structure of length $2L$, centered about $x=0$ with $V(x=-L)=0.0$ and $V(x=L)=V_{\text{applied}}$, or for a structure of length L , where $V(x=0)=0$ and $V(x=L)=V_{\text{applied}}$. The capacitance is obtained via Kroemer et al¹, as follows.

From Poisson's equation the change in density, $\delta\rho(x)$, subject to the change in applied potential energy, $\delta V(L)$, at $x=L$, yields a net change in charge density:

$$(3) \quad \delta Q(L) = -e \int_{-L}^L dx \delta\rho(x).$$

The differential capacitance is:

$$(4) \quad C(V) = \frac{e\delta Q(L)}{\delta V(L)} \equiv \frac{e}{\langle x \rangle},$$

which provides an implicit definition of $\langle x \rangle$. From Poisson's equation:

$$(5) \quad \langle x \rangle = \frac{\delta V}{\delta [dV(x=L)/dx]}.$$

¹ H. Kroemer, W. Chien, J. S. Harris, Jr. And D. D. Edwall, *Appl. Phys. Letts.*, **36**, 295 (1980).

and the 'width' of the capacitor is determined by the ratio of the change in applied potential energy at the boundary to the change in field at the boundary.

The carrier density is reconstructed from standard textbook expressions ²,

$$(6) \quad N_{reconstructed} = 2N_{ref} L_D^2 \left(\frac{d \langle x \rangle^2}{d\beta V} \right)^{-1}$$

where $\beta = (k_B T)^{-1}$, and L_D is the Debye length:

$$(7) \quad L_D^2 \equiv \frac{\epsilon}{\beta e^2 N_{ref}}$$

N_{ref} is a reference density. For a uniform structure $N_{reconstructed} = N_{ref}$.

Equation (5) is routinely used as an adjunct to experiments, to obtain information about doping profiles, offset voltages, etc. A reverse analysis is also pursued where an assumed device configuration is assumed and the C - V relationship is obtained. The resulting C - V is then compared to experiment where the closest fit is pronounced as the design of the structure under study. Thus, as indicated above, the results are dependent upon the physics used to represent the device under consideration. We work under the assumption that the analysis with the most representative quantum physics will provide a measure of the efficacy of the approach.

To illustrate the calculation we consider structures that are uniformly and nonuniformly doped. The first set of results is for a uniformly doped devices. For each heterostructure configuration three groups of figures are shown:

(i) *The first group* displays the heterostructure configuration, the reconstructed density, and the flat band density obtained from the Liouville equation;

(ii) *The second group* displays CV from which the reconstructed density is obtained;

(iii) *The third group* displays a plot³ (including blow-ups) of $\langle x \rangle^2 L_D^{-2} (2\beta)^{-1}$ versus $V_{applied}$, whose slope from equation (5) yields the

² See, e.g. D. K. Schroder, *Semiconductor Material and Device Characterization*, John Wiley & Sons, Inc. NY (1990), Equation (2.5b).

reconstructed density. Then from the combined $C-V$ and $\langle x \rangle^2 L_D^{-2} (2\beta)^{-1}$ curves we obtained the reconstructed density versus $\langle x \rangle$.

Several features are common to all configurations: (i) Qualitative features of the density profile are represented by the reconstruction. (ii) The magnitudes of the reconstructed density overestimate the minimum density.

For the uniform background density calculations the CV calculations have been performed for a variety of barrier height configurations, as well as with different effective masses. The code has been generalized to include variations in effective mass, and it is now possible to include simple band structure variations.

2.2 Low/High/Intermediate Uniform N_0 Heterostructure

For the uniform background doping calculation the background density is equal to $10^{18}/\text{cm}^3$. Those regions of the curve C^{-2} vs V that are parallel to the comparable curve for a structure without heterolayers (and not corrected for statistics), indicate a density equal to the background density, departures signify local charge accumulation or depletion.

Within any given configuration the displacement of the intersection of the C^{-2} vs V curve from the origin signifies a mean thermal and density dependent contribution, arising from the use of Fermi statistics. A displacement of a linear section of C^{-2} vs V , from another linear section of the curve, represents the offset voltage.

Figure 1a displays a comparison of the reconstructed and true density under flatband conditions for a 2000Å heterostructure (only the central 1400Å region is shown) with respectively, a 100mev barrier 800 Å wide preceded by a 200mev, 200Å barrier. The flatband distribution, $N_{\text{true}}(x)$, is obtained from the diagonal component of the density matrix (the analysis is discussed in a later section) and displays excess charge on either side of the taller barrier, with the greatest excess occurring at the region of larger offset voltage.

Comparing $N_{\text{reconstructed}}(\langle x \rangle)$ and $N_{\text{true}}(x)$ we see that the reconstructed density faithfully represents the qualitative features of the flat band profile. But there are troubling features that appear in many of the calculations (some of which have been discussed by others³): $N_{\text{reconstructed}}(\langle x \rangle)$ underestimates the

³H. L. Grubin, T. R. Govindan and M. A. Strosio, *Semi. Sci. Technol.* To be published.

accumulation of carriers closer to the reverse bias boundary and overestimates the accumulation layer further into the structure. The numerical calculations also reveal new quantum contributions at the reverse bias boundary arising from gradients in the density which lead to large values of *quantum potential*. These contributions are not shown in the diagrams, but generally lead to a reconstructed density that is approximately 50% larger than the background density for approximately 100 Å from the boundary surface. The significance of these terms will be discussed later in connection with some detailed modeling of the Schottky barrier interface.

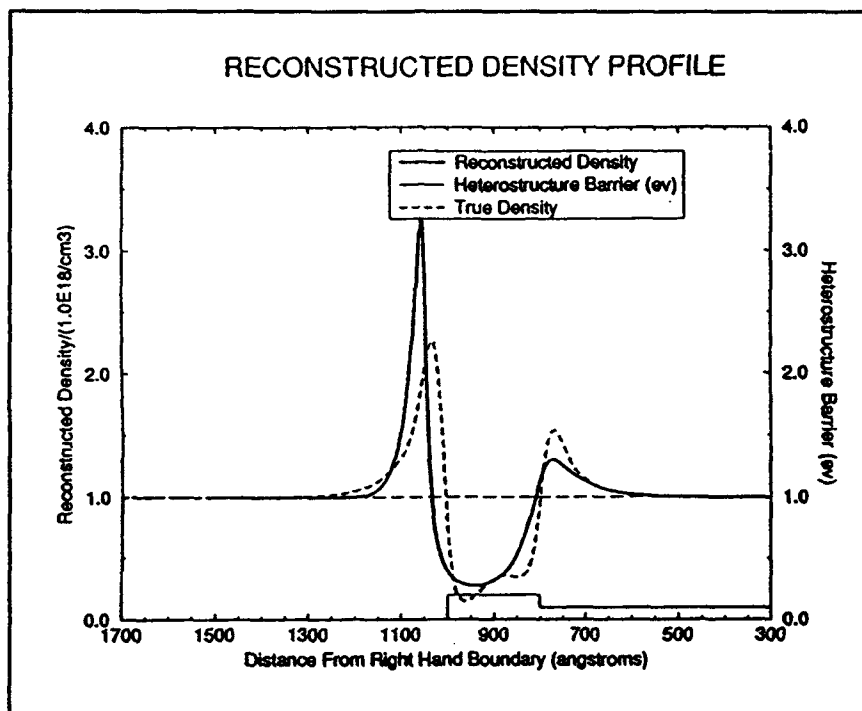


Figure 1a. Reconstructed density and density as obtained from the diagonal component of the density matrix for an asymmetric barrier structures. Nominal density is uniform and equal to $10^{18}/\text{cm}^3$.

All structure in the reconstructed density arises when the CV relation departs from that associated with depletion layer theory for uniform structures. CV for this structure is shown in figure 1b, where the vertical lines represent that

value of applied voltage at which $\langle x \rangle$ reaches the beginning and end of the wider barrier. The steepest slope compared to the depletion layer theory for uniform structures (dashed lines of figure 1b) occurs *within* the region of the wide barrier, where the density is lowest. On *either side of the wide barrier* the slope is smaller than that of depletion layer theory for uniform structures and there are regions of local charge accumulation.

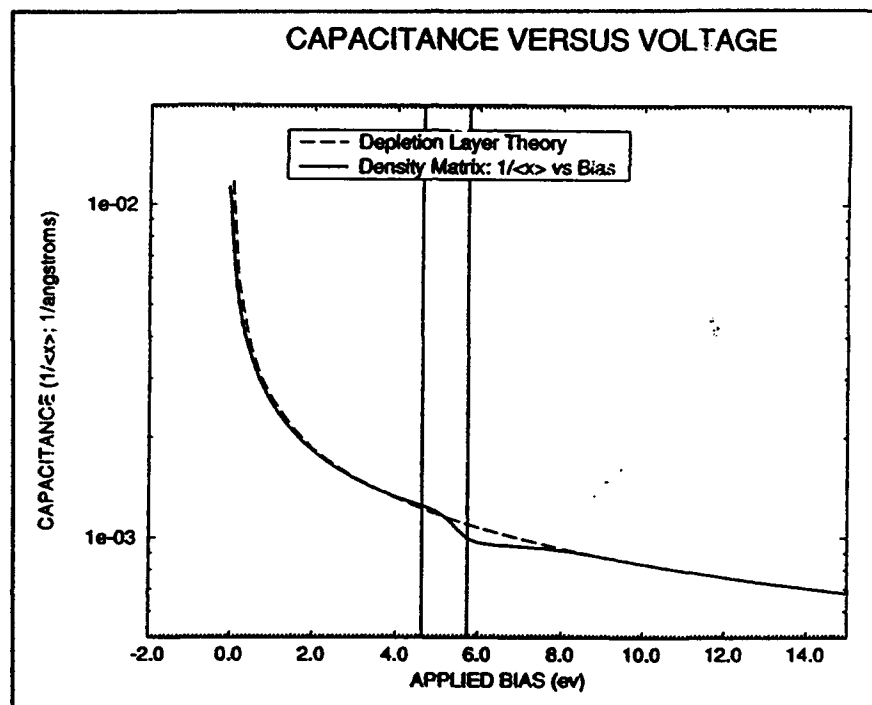


Figure 1b. Capacitance versus voltage for the calculation of figure 1a.

$N_{\text{reconstructed}}(\langle x \rangle)$ is obtained from the slope of C^{-2} vs V . C^{-2} is proportional to $\langle x \rangle^3$, and in figure 1c we show $\langle x \rangle^2$ vs V ; providing the most dramatic effect of the variations of charge on the capacitance. There are several points to note. First, note the dashed curve in the center of the diagram, and imagine this curve extend across the diagonal of the figure. The normalized derivative of this curve with respect to the applied voltage yields the reference density. Next imagine the presence of three lines representing the asymptotic slopes to the curves. The low bias curve, beginning at approximately 4 eV possesses a slope smaller than that of the diagonal, indicating with reference to equation (5), a region of charge accumulation. At this voltage $\langle x \rangle$ is beginning to

reach the heterostructure. The intermediate bias curve displays a slope considerably in excess of the diagonal line, indicating according to equation (5) a region of charge depletion. The high bias curve displays a slope less than that of the low bias curve, signifying charge accumulation in excess of the low bias value. The consequences of these results is shown in figure 1a.

The dashed curve in figure 1a is a result of the calculation from the density matrix in the coordinate representation. The integrated charge density, including the background charge is zero. While we have not calculated the net charge from the reconstructed density, it appears as though the net integrated charge density is zero.

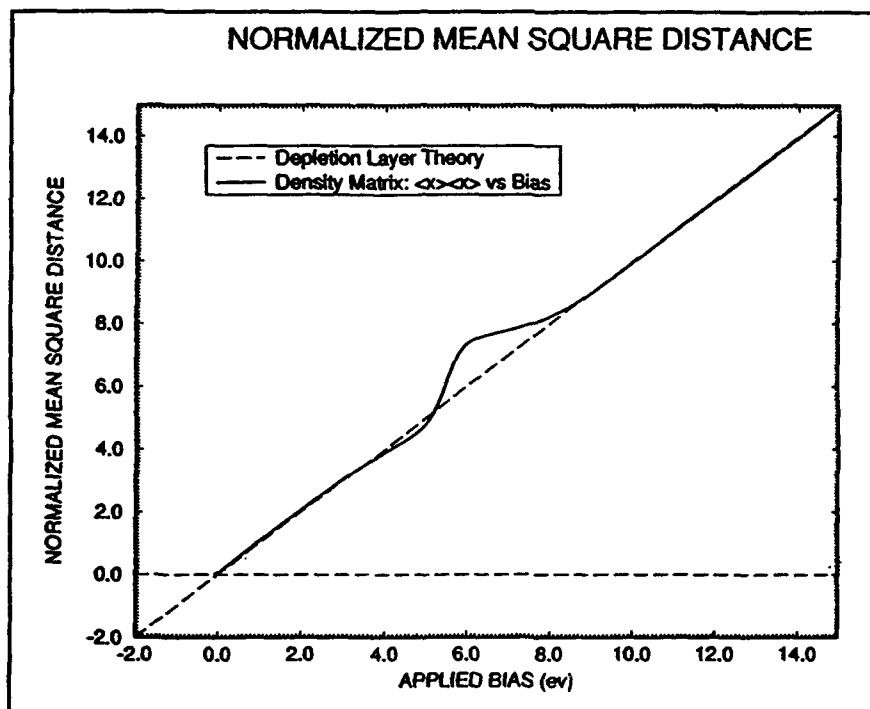


Figure 1c. Normalized mean square distance versus voltage for the calculation of figure 1a.

We note that the dashed line in figure 1a is obtained under flat band conditions. From a computational point of view, this means that a voltage difference must be imposed between the source and drain contacts equal to the difference in barrier heights at the ends of the structure (in this case 100 meV). Now standard theories from the depletion layer approximation with Boltzmann

statistics indicate that the normalized $\langle x \rangle^2$ for uniform density varies as $V_{\text{applied}} + k_B T$. For the situation where there is a difference in the barrier heights between the cathode and anode portions of the structure we expect this difference to appear in the intercepts of $\langle x \rangle^2$ at low and high bias levels. To determine it this was the case we enlarged the *extrapolated* bias intercept points at low and high bias, as shown respectively in figures 1d and 1e. At low bias levels the intercept is approximately 65mev to the left of the origin. At high bias levels the intercept is approximately 40mev to the right of the origin. The net displacement between the low and high voltage intercepts is approximately 105 mev, which is near the 100 mev barrier height of the long barrier. These results appear to be independent of the height of the middle barrier.

At high bias where there is no offset voltage expected, the existence of a nonzero bias intercept arises from the statistics of the calculation. If Boltzmann statistics were imposed an intercept of $k_B T$ would be expected. For Fermi statistics the intercept occurs at the mean energy of the entering carriers.

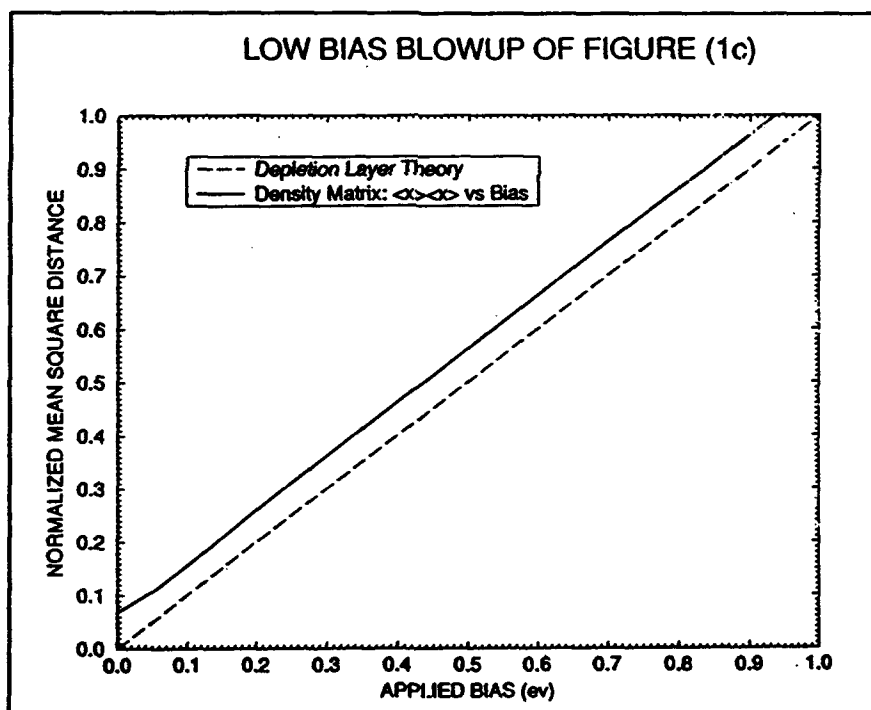


Figure 1d. Low bias blow up of the normalized mean square distance versus voltage for the calculation of figure 1c.

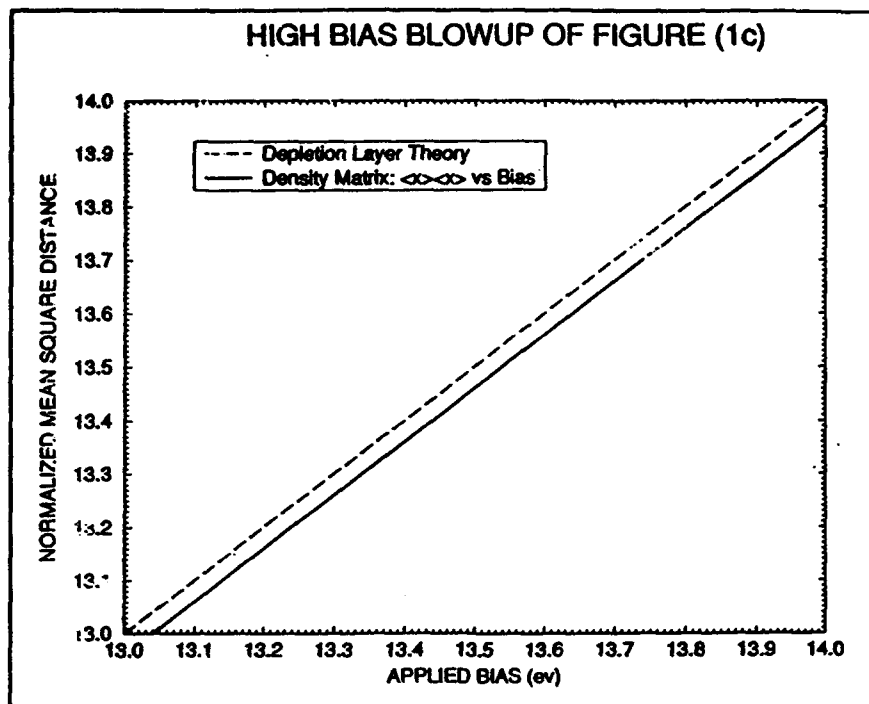


Figure 1e. High bias blow up of the normalized mean square distance versus voltage for the calculation of figure 1c.

2.3 Double Barrier Uniform N_0

The next sequence of calculations is for a double barrier resonant tunneling diode uniformly doped to $10^{18}/\text{cm}^3$. Figure 2a displays the position of the double barriers (lower solid lines). The barriers are each 100Å wide, 300mev high, and separated by a 100Å quantum well.

The equilibrium solution displays a charge density within the quantum well that exceeds the background doping. As in figure 1a $N_{\text{reconstructed}}(<x>)$ is initially lower in value than that obtained from the density matrix. The remaining two peaks in the reconstructed density are higher in value than that obtained from the density matrix. This feature was also present in figure 1a. Of equal significance is that the peaks are displaced from the values obtained from the equilibrium density matrix calculation.

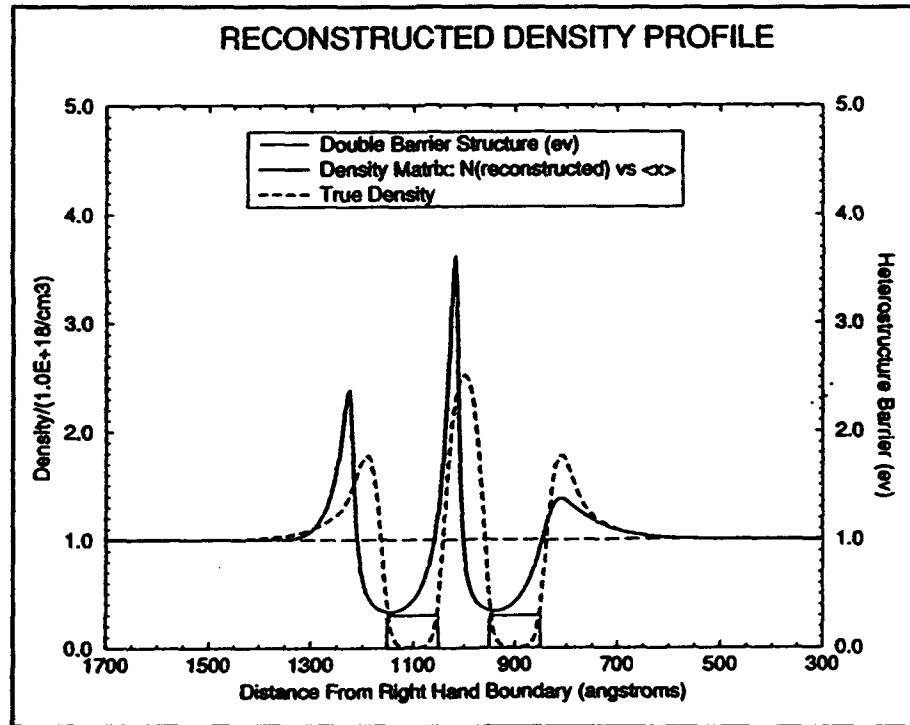


Figure 2a. Reconstructed density and density as obtained from the diagonal component of the density matrix for a double barrier structures. Nominal density is uniform and equal to $10^{18}/\text{cm}^3$.

The CV profile is shown in figure (2b) where the vertical lines again delineate the values of bias where $\langle x \rangle$ reaches the beginning and ends of the heterostructure. At low and high values of bias CV obtained from depletion layer theory for uniform structures overlaps the computed CV and attest to the fact that there is a zero offset voltage at the ends of the device. The steeper and shallower slopes within the heterostructure region relate to accumulation and depletion in the heterostructure region as in figure 1. matrix calculation.

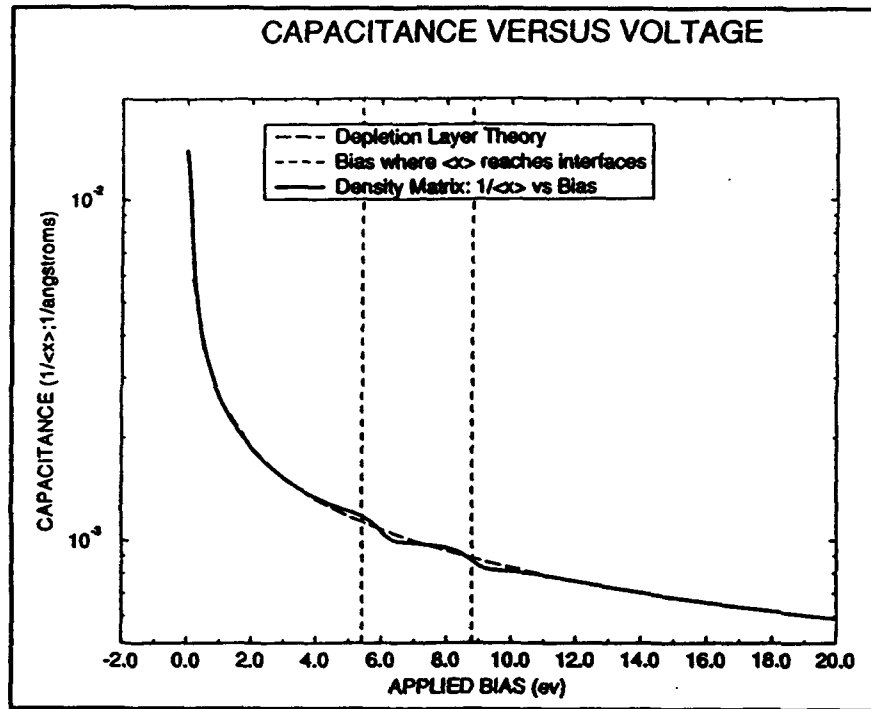


Figure 2b. Capacitance versus voltage for the calculation of figure 2a.

The normalized $\langle x \rangle^2$ vs. V is displayed in figure (2c), and similar structure is seen in the regions corresponding to charge depletion as well as accumulation. In particular note that there are three regions where the slope of $\langle x \rangle^2$ vs. V is smaller than that of the diagonal and two regions where the slope is greater than the diagonal. The three regions of reduced slope correspond to local charge accumulation, while the two regions of increased slope correspond to charge depletion.

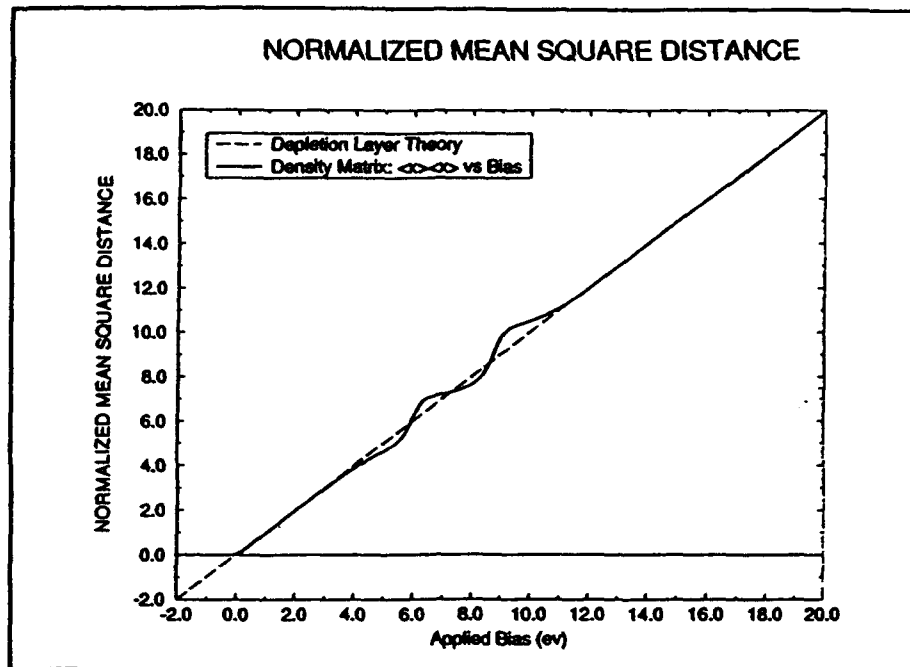


Figure 2c. Normalized mean square distance versus voltage for the calculation of figure 2a

Unlike the calculation of figure 1 where there was a heterostructure difference between the cathode and anode sides of the structure, the figure 2 calculation sustains no such difference. It is anticipated that there will be no offset between the high and low bias portions of the curves of figure 2c. Figures 2d and 2e display blowups of these regions. As seen these figures show approximately equal displacements, indicating a zero offset voltage.

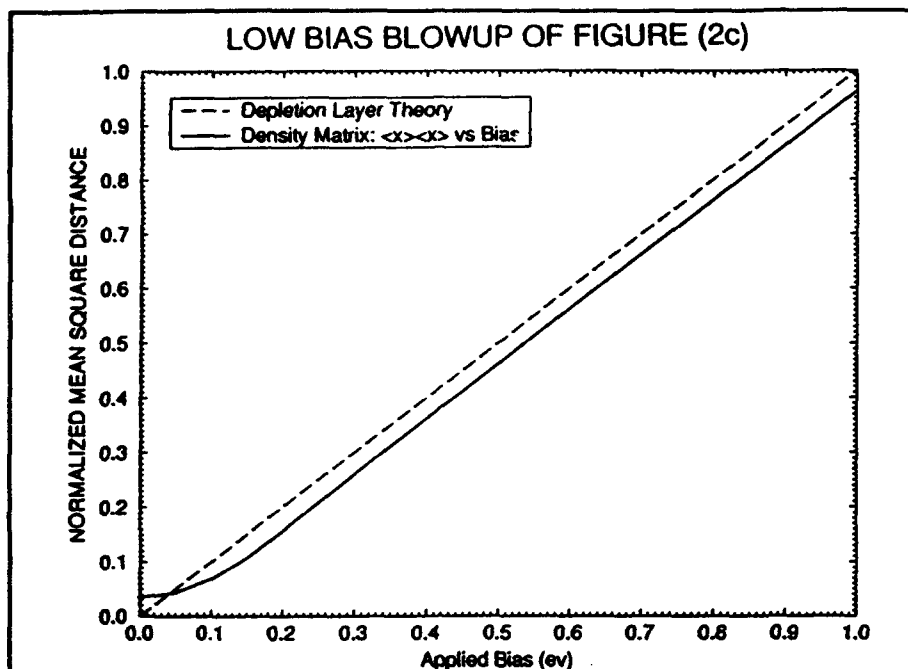


Figure 2d. Low bias blow up of the normalized mean square distance versus voltage for the calculation of figure 2c.

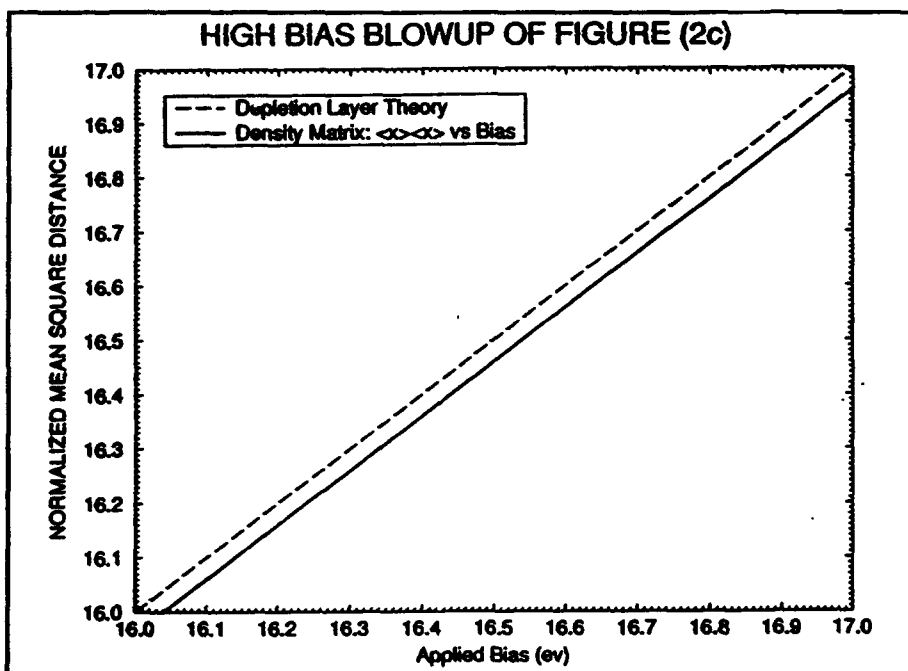


Figure 2e. High bias blow up of the normalized mean square distance versus voltage for the calculation of figure 2c.

2.4 Staggered Heterostructure Uniform N_0

The third study is for the staggered heterostructure as shown in figure 3a. This case treats the case where there is a heterostructure difference between the cathode and anode portions of the structure, and there is a central region where local flat band conditions occur. This structure consists of (i) a 300mev barrier extending from the right boundary to a point 700 Å into the structure, followed by (ii) a 150mev barrier extending another 700 Å into the structure.

The non self-consistent potential energy distribution is shown by the solid lines at the bottom of the diagram. For this structure and a doping of $10^{18}/\text{cm}^3$ the charge distributions at the heterostructure interfaces are independent of and replicate each other. The self-consistent potential distribution reflects this charge distribution, and the self consistent potential at the ends of the structure and over a considerable region within the center of the device is equal to zero. The real space transfer at the heterostructure interfaces are all the same. The replication will be modified when holes and the relevant energy gap variations are included.

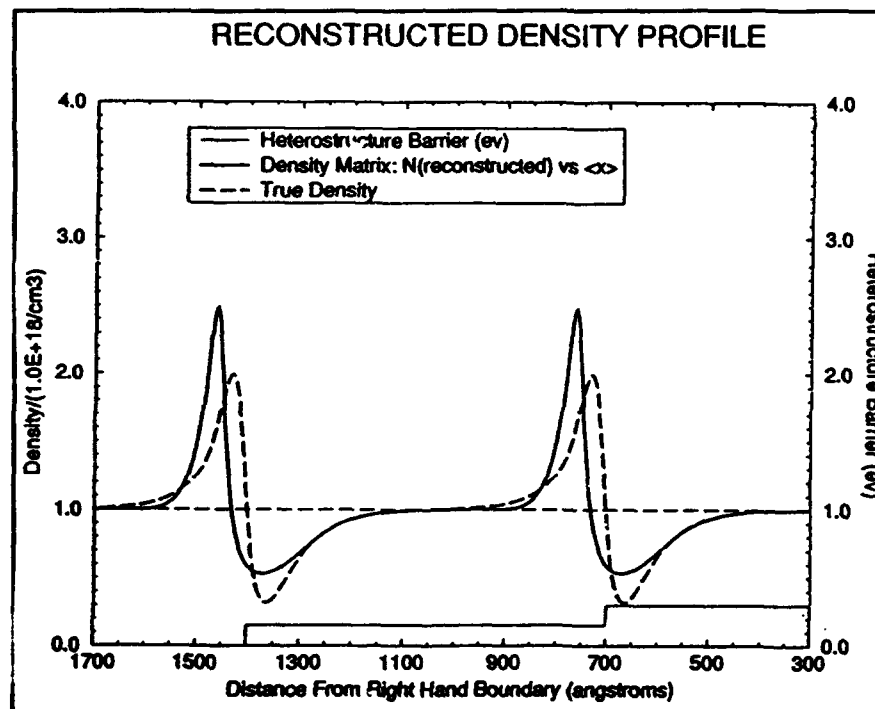


Figure 3a. Reconstructed density and density as obtained from the diagonal component of the density matrix for a staggered heterostructure. Nominal density is uniform and equal to $10^{18}/\text{cm}^3$.

Unlike the earlier reconstructed density calculations studies where the depletion zone $\langle x \rangle$ initially reached a region of charge accumulation, in figure 3a the initial region is one of charge depletion, followed by charge accumulation. As in the previous discussion the peak reconstructed density is both greater than and displaced from the peak as obtained from the flatband solutions to the Liouville equation in the coordinate representation.

Figure 3b displays CV where the vertical lines denote the bias values at which $\langle x \rangle$ reaches the beginning and ends of the center heterointerface.

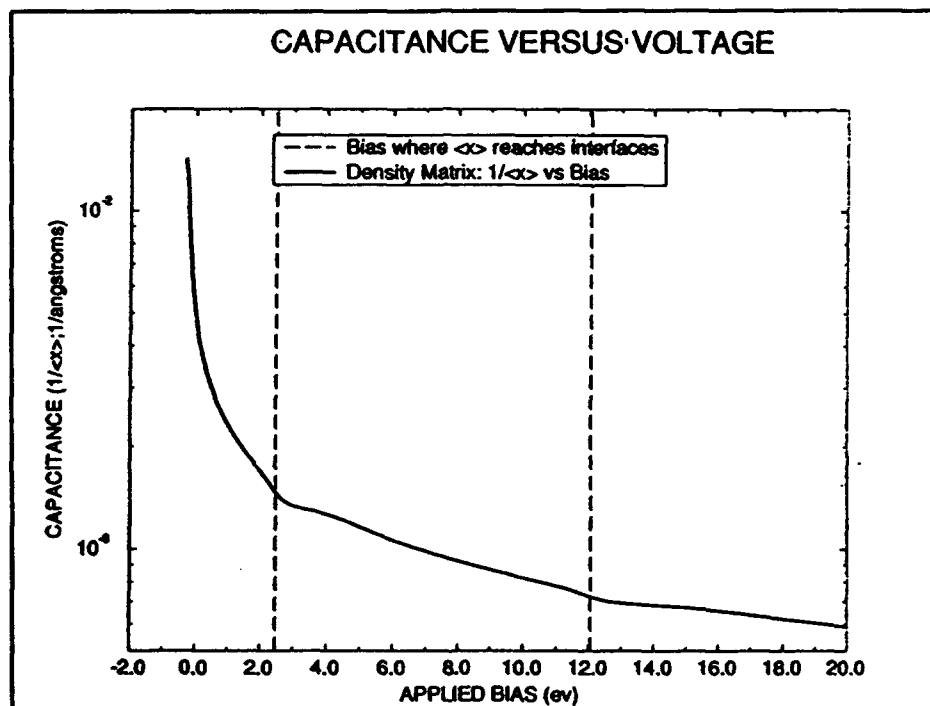


Figure 3b. Capacitance versus voltage for the calculation of figure 3a.

The normalized $\langle x \rangle^2$ vs. V is displayed in figure 3c. Note the two isolated regions. For both of these regions the initial slopes are positive and equal in value and correspond to a decrease in value for the reconstructed density. three regions where the profile is flat and parallel to the uniform density line. As a function of bias the gradient of $\langle x \rangle^2$ first exceeds that associated with the flat profile and charge depletion occurs. This region is followed by a region where the slope, while positive, is smaller than that associated with the uniform profile,

signifying charge accumulation. Very similar structure appears at the higher bias levels. There are important points to note about these results. At the low bias levels, the applied bias range of local increase in $\langle x \rangle^2$ followed by a local decrease is smaller than at the higher bias levels. But the slopes are the same. The nonlinear relation between the results of these regions is a consequence of the nonlinear dependence of the depletion layer thickness as applied bias.

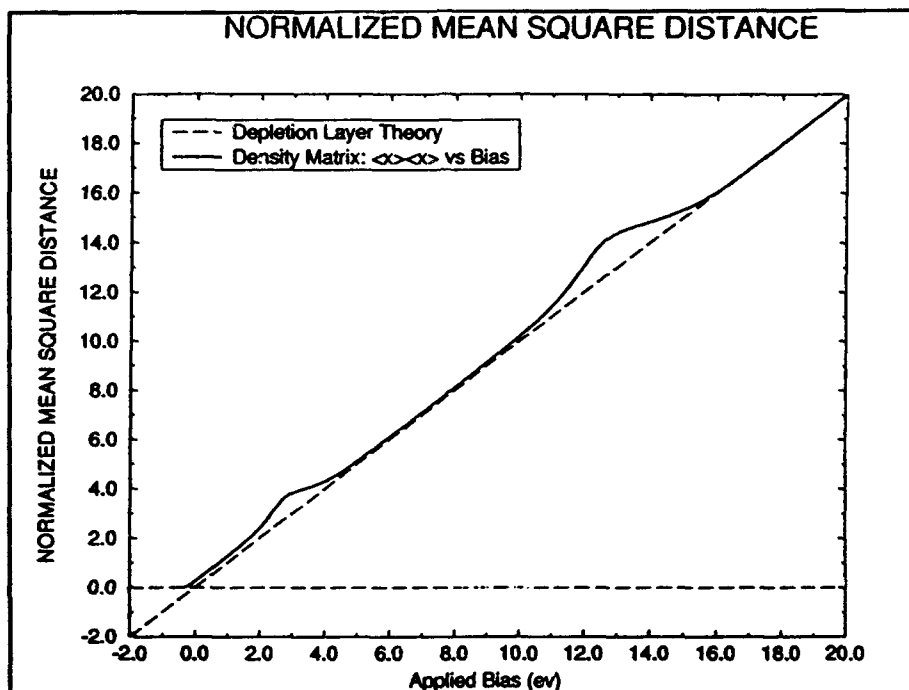


Figure 3c. Normalized mean square distance versus voltage for the calculation of figure 3a

There are differences in the heterostructure potential at the two ends of the structure and this is expected to manifest in differences in the intersection of the high intermediate, and low bias portions of the curves of figure 3c. Blowups of three regions as shown in figures 3d and figure 3f.

In the case of figure 3d, the bias levels correspond to $\langle x \rangle$ within the 300 meV barrier region, approaching and reaching the first heterostructure interface at 700 Å. The differences between the intercepts of the solid line representing changes in $\langle x \rangle$ along the 300 meV barrier region (view the top portion of the

intercept) and the diagonal dashed line representing the flat region is approximately 270 meV.

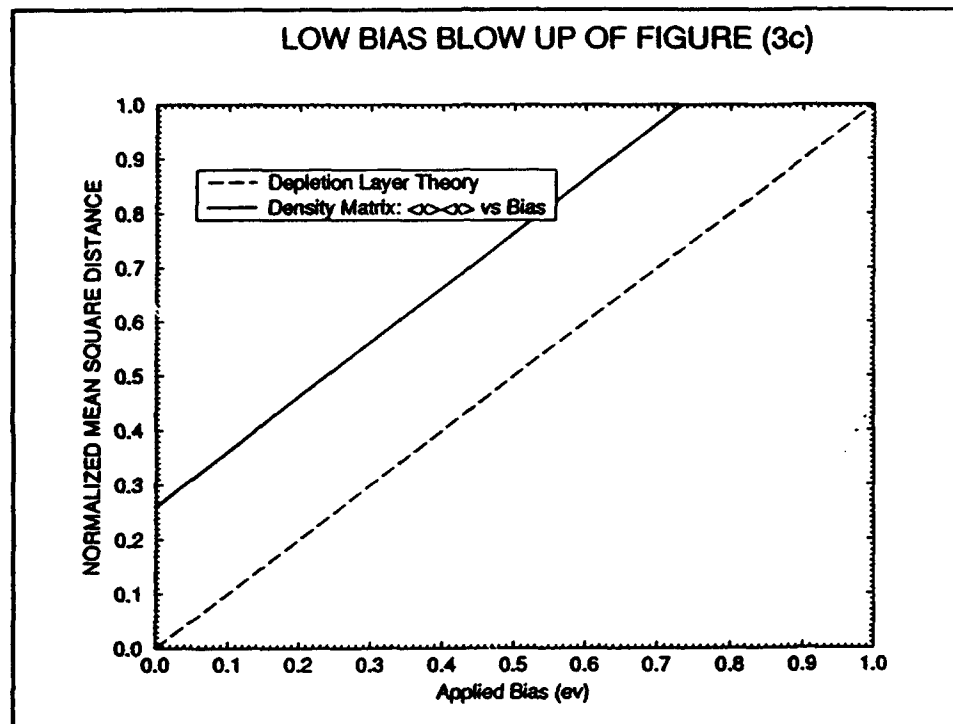


Figure 3d. Blow up of figure 3c for a range of applied bias levels within the 300 meV barrier region.

In figure 3e the bias levels are such that $\langle x \rangle$ falls within the 150 meV region. The displacement of the introspect of the solid and dashed lines (again view the top most horizontal axis) is approximately 120 meV. For the final range of bias shown in figure 3f the displacement of the solid and dashed lines (again view the top most horizontal axis) is approximately -30 meV. The relative displacements of the solid and dashed lines follows the same qualitative behavior as that associated with figure 1. Further the net displacement between the right and left hand sides of the structure is approximately 30 meV, which is the difference in the values of the heterostructure barriers.

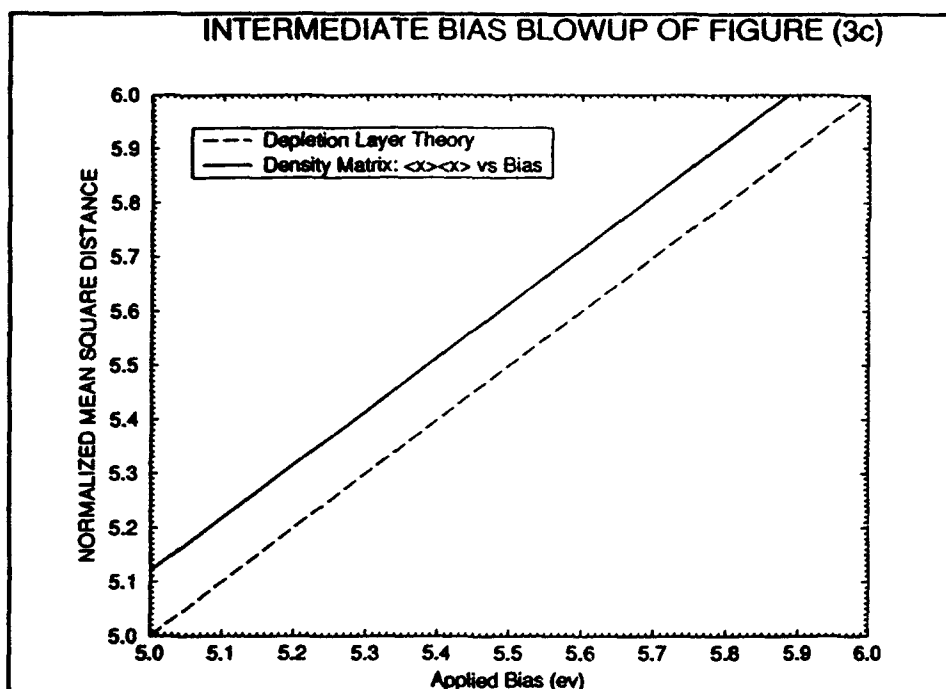


Figure 3e. Blow up of figure 3c for a range of applied bias levels within the 150 mev barrier region.

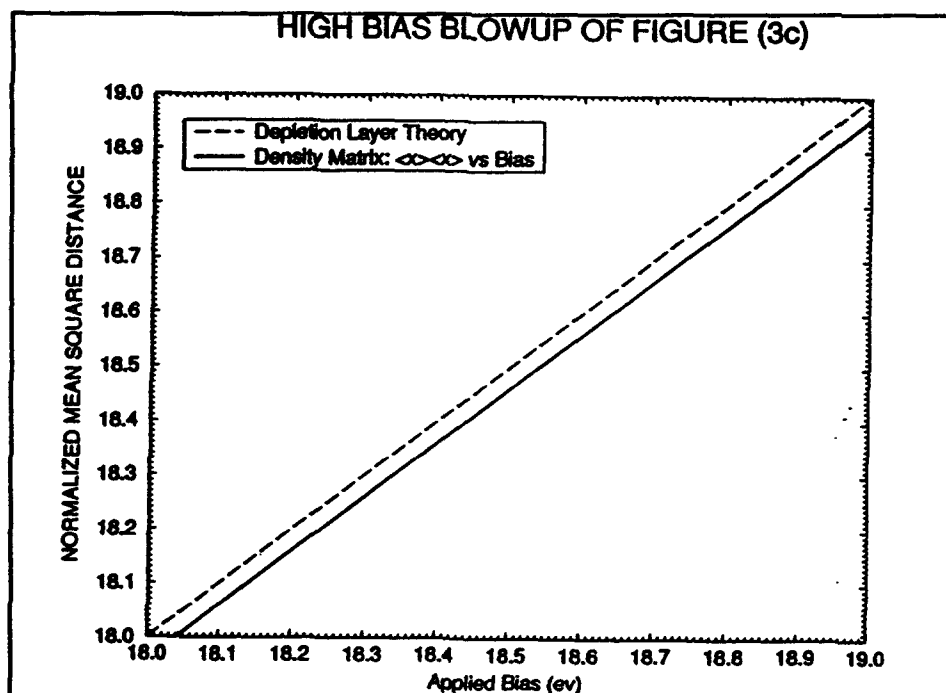


Figure 3f. Blow up of figure 3c for a range of applied bias levels within the 0.0 mev barrier region.

2.5 Single Barrier, Nonuniform N_0

Additional calculations have been performed with variations in background density. In the calculation discussed below the Liouville equation in the coordinate representation was coupled to Poisson's equation for a 2000 Å long structure, nominally doped to $10^{18}/\text{cm}^3$, with a 150 Å, 300 meV barrier within a 300 Å, N⁺ region. The density and potential energy at equilibrium are shown at equilibrium figure 4a⁴, note the change in dimensions to meters and nanometers.

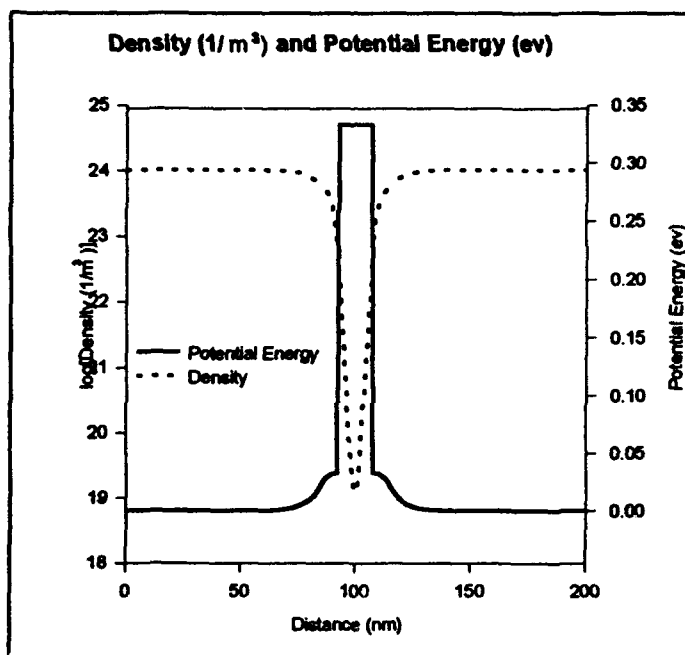


Figure 4a. Equilibrium distribution of density, from the density matrix, and potential energy for a single barrier located within an N⁺ region.

⁴D. K. Ferry and H. L. Grubin, A chapter to appear in *Solid State Physics*, Academic Press (1994).

The reconstructed density as well as the density computed from the quantum Liouville equation in the coordinate representation are shown in figure 4b.

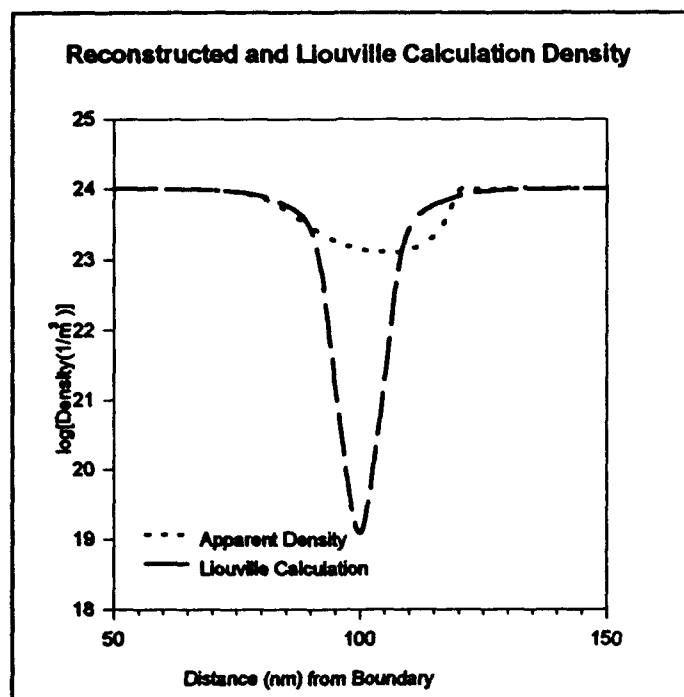


Figure 4b. Reconstructed density and density as obtained from the diagonal component of the density matrix for a single barrier structure with a 300 Å region in the center of the structure.

There are several points of note. First, the minimum value of the reconstructed is orders of magnitude higher than that computed from the density matrix, although on a linear plot the apparent difference would appear to be smaller. Second there is a region in which the minimum in the reconstructed density is smaller than that obtained from the Liouville equation. Again, while the net charge density has not been computed it appears that the integrated charge density obtained from the density matrix, and that from the reconstructed density are the same.

The reconstructed density is obtained from the derivative of $\langle x \rangle^2$ versus applied bias, which is shown in figure 4c. According to equation (6) the slope of $\langle x \rangle^2$ determines the reconstructed density. In the calculation, the central region

was approximately three orders of magnitude smaller in doping than the cladding region. Thus if the low doped region was long enough for the density to approach its background value, the slope of $\langle x \rangle^2$ versus V_{applied} would be correspondingly three orders of magnitude higher at the higher bias levels than at the low bias levels. Debye tailing would determine that rate at which this high slope would be reached. For the situation of figure 4, with particular attention to figure 4c, where the normalized $\langle x \rangle^2$ versus V_{Applied} is displayed, the rate at which the slope is increased is accelerated by the presence of the barrier. And it is anticipated that increases in the barrier height would result in a larger slope. In figure 4c we have drawn a line tangent to the slope within the depleted region. The intersection of this line with the two dotted lines provides a measure of the bias need to move $\langle x \rangle$ across the barrier-plus- N^- region. Thus it appears that the CV measurement will yield information about the position of the barrier; it is not clear that information about the height of the barrier can be obtained using this technique.

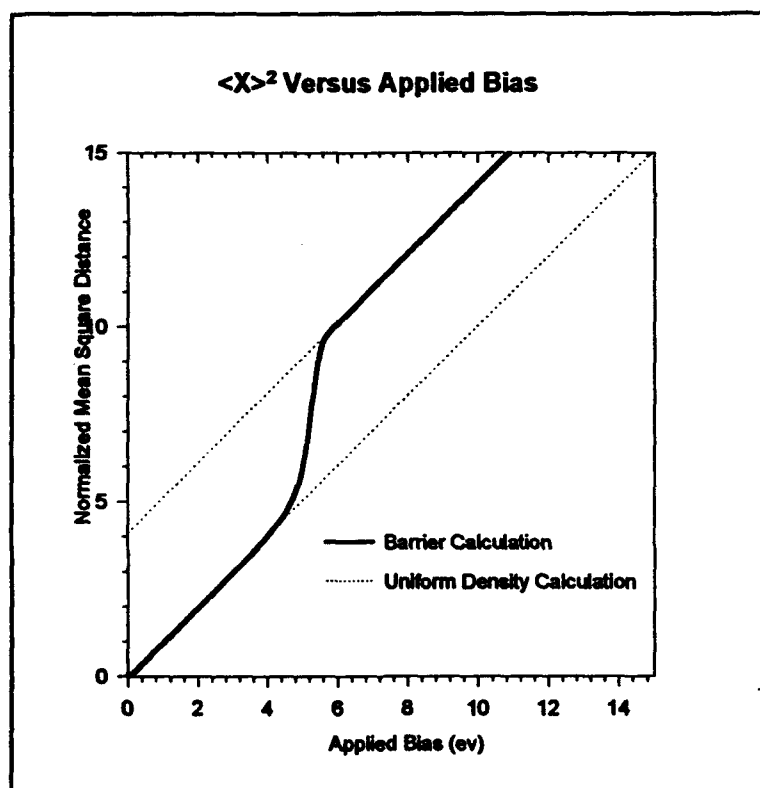


Figure 4c. Normalized mean square distance versus volage for the calculation of figure 4a.

3. DISSIPATION CALCULATIONS-

3.1 Introduction to the Phenomenological Model

The *CV study* discussed in the previous section was developed under conditions of zero current flow. While under reverse bias conditions it is expected that the nonzero component of current would be leakage current, capacitance values are normally required under nonequilibrium conditions when current is flowing. For example in a typical FET small signal analysis is generally performed on structure that are already subject to a finite bias, from which a nonlinear bias dependent capacitance is obtained. To perform similar calculations with the density matrix program requires at least two ingredients:

- (i) First we need a procedure for calculating current;
- (ii) Second we need a more realistic representation of the contact boundary condition.

Both of the above features is discussed below, using a phenomenological model for the calculation of current.

With current flow, the density matrix is complex, and we have assumed boundary conditions corresponding to either a displaced Fermi-Dirac or Maxwellian distribution function, with current obtained from the condition that all of the energy supplied by an external source is dissipated within the device. (We note that problems including a solid-vacuum interface, such as in vacuum microelectronics applications, would not satisfy this condition.)

Current was calculated using several different models. Initially *IV* was obtained using scattering contributions which at low energies was obtained from Fokker Planck dissipation⁵. *Current was obtained from a condition in which the mean applied and dissipated energies were equal.* At higher energies, within a phenomenological description, a scattering potential (discussed in section 4) was introduced whose structure reduces, at low energies to Fokker-Planck dissipation. More generally the scattering potential behaves like a quasi-Fermi energy which

⁵ M. A. Strosio, *Superlattices Microstruct.* 2, 83 (1986).

undergoes a significant change in the vicinity of a heterointerface, in the spirit of Grinberg and Luryi ⁶.

The *phenomenological model*, discussed in section 3, in terms of a quasi-Fermi energy, and illustrated below, does not provide any details associated with the specific electron phonon interaction as discussed by others⁷.

3.2 The Phenomenological Model: Single barrier, constant scattering time.

We illustrate the model with recently presented calculations⁸, figure 5, is for a 2000Å structure centered about the origin containing a single 300 meV high, 100Å wide barrier embedded within a 300Å N⁻ region, surrounded by uniformly doped $10^{18}/\text{cm}^3$ material. The scattering time τ is constant and equal to 10^{-13}sec . The first three figures show potential energy, charge, and quasi-Fermi energy distributions, respectively, for different bias levels. From figure (5a) as the collector boundary is made more negative with respect to the emitter, a local 'notch' potential well forms on the emitter side of the barrier. The potential energy decreases linearly across the barrier, signifying negligible charge within the barrier, followed by a broad region where the energy decreases to its value at the collector. The charge distribution, figure (5b) displays a region of local accumulation on the emitter side of the barrier, followed by a broad region of charge depletion on the collector side. Both results are consistent with the experimental findings of Eaves et al. ⁹. Significant amounts of charge accumulation are apparent at bias levels beyond 300 meV.

⁶ A.A. Grinberg and S. Luryi, *IEEE Trans. Elect. Devices*, 40, 859 (1993).

⁷ Key papers of relevance to the proposed study include: (1) N. Mori and T. Ando, *Phys. Rev. B* 40, 6175 (1989); (2) K. W. Kim and M. A. Stroscio, *J. Appl. Phys.* 68, 6289 (1990), (3) A. R. Bhatt, K. W. Kim, M. A. Stroscio, G. J. Iafrate, M. Dutta, H. L. Grubin, R. Haque and X. T. Zhu, *J. Appl. Phys.* 73, 2338 (1993); (4) P. J. Turley and S. W. Teitsworth, *J. Appl. Phys.* 72, 2356 (1992).

⁸ D. K. Ferry and H. L. Grubin, *Proc. International Conference on Computational Electronics*, Leeds, UK, 247 (1993).

⁹ See, e.g. L. Eaves, F. W. Sheard and G. A. Toombs, in *Physics of Quantum Electron Devices*, F. Capasso, ed., Springer-Verlag Berlin, 107 (1990).

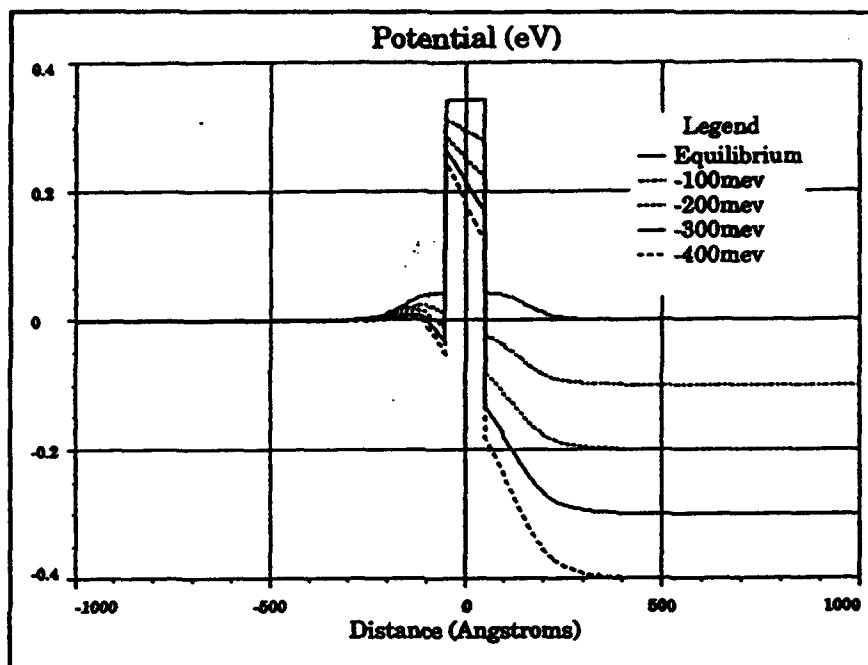


Figure 5a. Bias dependence of the potential energy for a single barrier 100Å wide, 300 meV high.

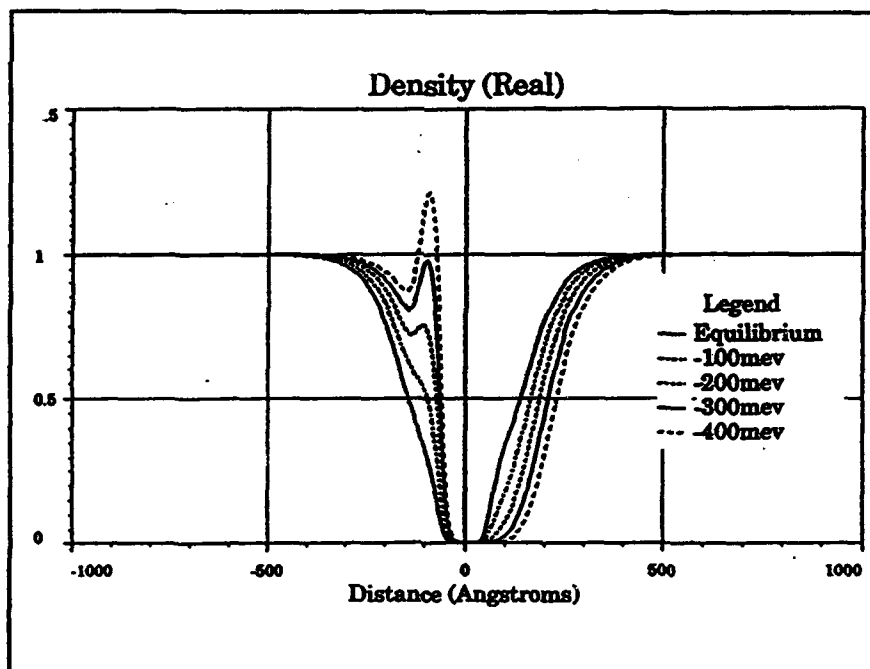


Figure 5b. Bias dependence of the density for a single barrier 100Å wide, 300 meV high.

For the figure 5 calculation, the quasi-Fermi energy (relative to the equilibrium Fermi energy), which is introduced into the governing equations as discussed in section 4, was computed from:

$$(7) \quad E_F(x) = -mj \int_{-L}^x \frac{dx'}{\rho(x')\tau(x')}$$

whose form will be justified below. In equation (7), $j = \rho(x)v(x)$ is the velocity flux density, $\rho(x)$ is the electron density, $\tau(x)$ a relaxation time. The velocity flux density, satisfies current continuity conditions and is independent of position. Current is $-ej$. As seen from figure (5c), E_F is approximately equal to the zero within the first half of the barrier (although in the emitter region the variation in E_F matches that of $V(x)$, and insures that $\rho(x)$ is constant in the vicinity of the emitter boundary) and then drops to a value approximately equal to the bias through the remaining part of the structure.

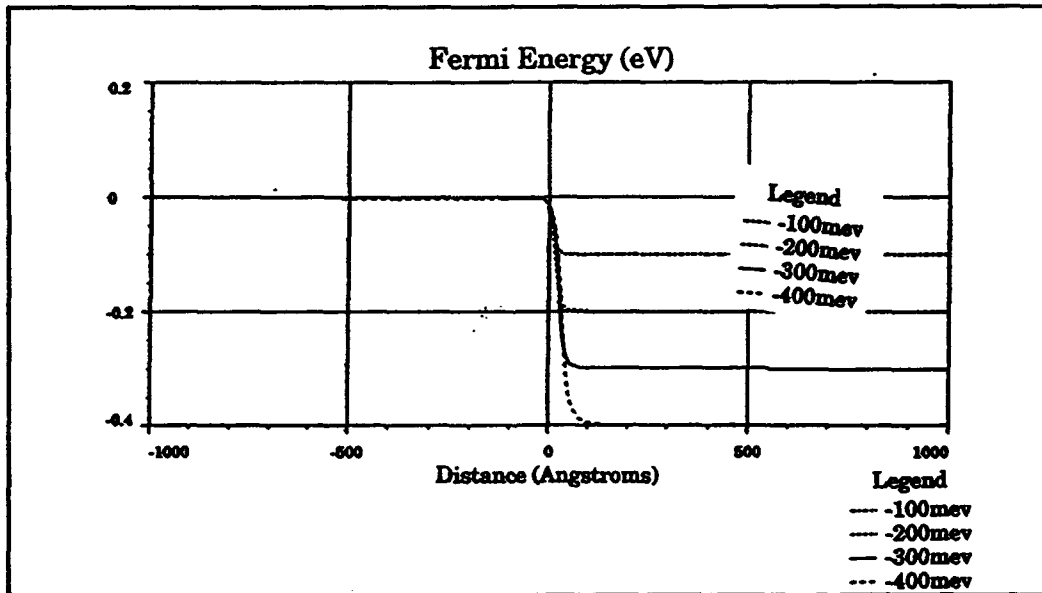


Figure 5c. Bias dependence of the quasi-Fermi energy for a single barrier 100Å wide, 300 meV high.

IV for the 150Å barrier is shown in figure (5d), along with, for comparison a calculation for a 100Å wide barrier (same barrier height). The inset displays the same results on a logarithmic plot. The significant differences between the two

are: (1) the shape of the curve at the lower bias levels, and (2) the magnitude of the current. For the wider barrier the current at low bias is almost two orders of magnitude smaller.

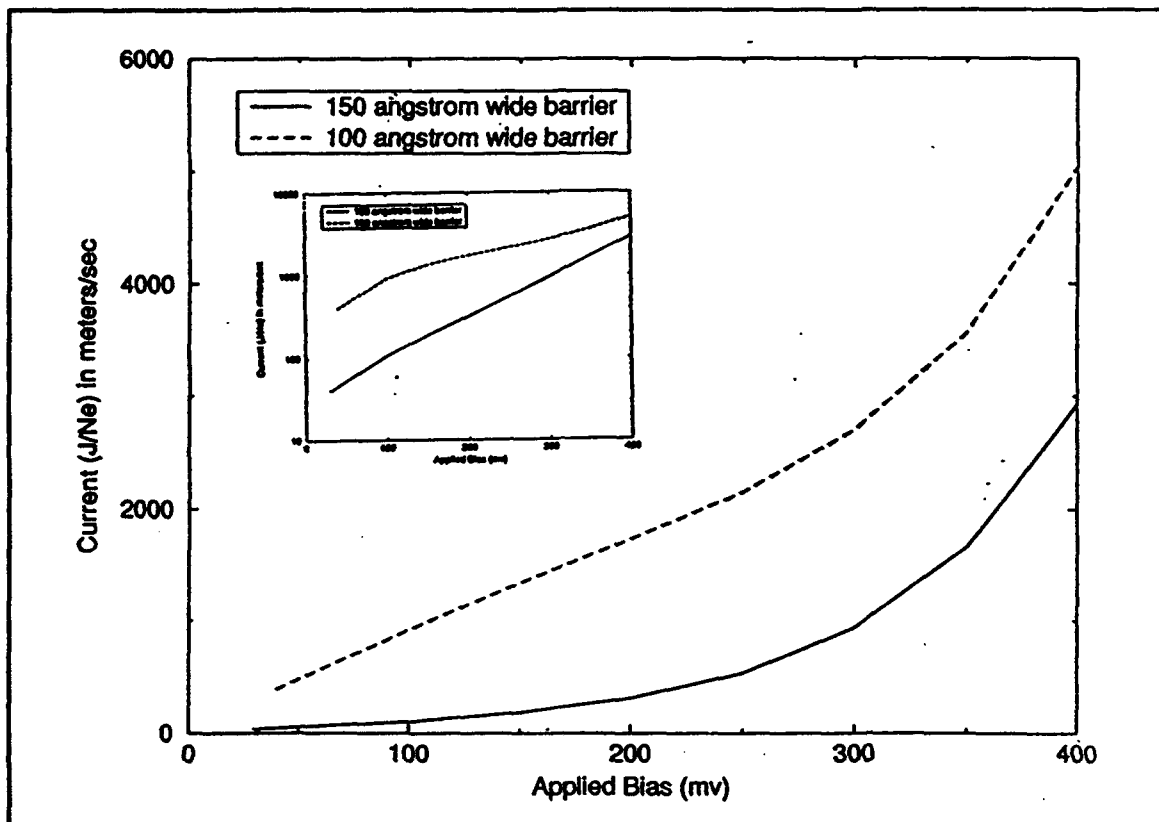


Figure 5d. Current versus voltage for a single barrier structures.

In the IV calculations the field in the emitter region and the current are related by a mobility law, which is specified once the scattering time, τ , is set. Thus the difference in the current values, for the narrow and wide barrier structures, reflects a value of the emitter region electric field that is smaller for the 150Å wide barrier structure and that more of the potential energy falls across the barrier for a given bias, then is the case with the 100Å barrier. For the 150Å calculation, the current is dominantly thermionic and varies exponentially with voltage (the inset shows a linear behavior on a semilog plot). The narrower structure displays IV with a larger tunneling component and approximately linear behavior at low bias levels.

4. ETIOLOGY OF THE PHENOMENOLOGICAL DISSIPATION MODEL

4.1 The Quantum Liouville Equation

Initial work on dissipation incorporated Fokker-Planck mechanisms¹⁰. This took the following form:

$$(8) \quad \frac{\partial \rho}{\partial t} + \left(\frac{\hbar}{2mi} \right) (\nabla_x^2 - \nabla_{x'}^2) \rho(\mathbf{x}, \mathbf{x}', t) - \left(\frac{1}{i\hbar} \right) [V(\mathbf{x}, t) - V(\mathbf{x}', t)] \rho(\mathbf{x}, \mathbf{x}', t) \\ + \left(\frac{1}{2\tau} \right) (\mathbf{x} - \mathbf{x}') \cdot (\nabla_x - \nabla_{x'}) \rho(\mathbf{x}, \mathbf{x}', t) + \left(\frac{\Xi}{\hbar^2} \right) (\mathbf{x} - \mathbf{x}') \cdot (\mathbf{x} - \mathbf{x}') \rho(\mathbf{x}, \mathbf{x}', t) = 0$$

where τ represents a scattering time, and the term containing Ξ represents a diffusive term in the momentum representation. In reference [10], equation (2) was used to obtain quantum corrected energy and momentum balance equations; the term linear in $(\mathbf{x} - \mathbf{x}')$ provided *momentum relaxation*, while term quadratic in $(\mathbf{x} - \mathbf{x}')$ yielded *energy relaxation*. In the calculations of this proposal only scattering terms that were of odd-order in $(\mathbf{x} - \mathbf{x}')$ were considered, contributions of even-order in $(\mathbf{x} - \mathbf{x}')$ are presently being incorporated into DENMAT.

Equation (8) which includes Fokker-Planck dissipation needs justification for semi-conductor structures; this follows. The equation of motion for the density operator ρ_{op} , governed by the Hamiltonian H is:

$$(9) \quad i\hbar \frac{\partial \rho_{op}}{\partial t} = [H, \rho_{op}]$$

where the Hamiltonian contains dissipation mechanisms. The dissipation portion of the Hamiltonian $H_{dissipation}$ is written as:

$$(10) \quad i\hbar \left(\frac{\partial \rho}{\partial t} \right)_{dissipation} \equiv [H_{dissipation}, \rho_{op}]$$

¹⁰ H. L. Grubin, T. R. Govindan, J. P. Kreskovsky and M. A. Stroscio, *Solid State Electronics* (in press).

where dissipation is asserted to include momentum dissipation without any energy loss at well as energy dissipation through, e.g. phonon scattering. We note that $\rho(\mathbf{x}, \mathbf{x}') = \langle \mathbf{x} | \rho_{op} | \mathbf{x}' \rangle$.

While general approaches to scattering have been discussed by Iafrate and Krieger¹¹, and others¹² the approach we have taken developed from a generalization of classical scattering, within the framework of the Boltzmann transport equation, generalized for Wigner functions. The Wigner function and density matrix are related through a Weyl transformation. In particular, if scattering of the Wigner function is represented as¹³:

$$(12) \quad \left[\frac{\partial f_w(\mathbf{k}, \mathbf{x})}{\partial t} \right]_{\text{dis}} = -\frac{2}{(8\pi^3)} \int d\mathbf{k}' \{ f_w(\mathbf{k}, \mathbf{x})(1 - f_w(\mathbf{k}', \mathbf{x}))W(\mathbf{x}, \mathbf{k}', \mathbf{k}) - f_w(\mathbf{k}', \mathbf{x})(1 - f_w(\mathbf{k}, \mathbf{x}))W(\mathbf{x}, \mathbf{k}, \mathbf{k}') \}$$

then scattering of the density operator in the coordinate representation is obtained through application of the Weyl transformation:

$$(13) \quad \langle \mathbf{x} | \rho_{op} | \mathbf{x}' \rangle = \int d\mathbf{k} \langle (\mathbf{x} - \mathbf{x}') | \mathbf{k} \rangle f_w(\mathbf{k}, \frac{\mathbf{x} + \mathbf{x}'}{2})$$

which in the case of Boltzmann statistics is of the form

$$(14) \quad \left[\frac{\partial \langle \mathbf{x} + \frac{\mathbf{s}}{2} | \rho_{op} | \mathbf{x} - \frac{\mathbf{s}}{2} \rangle}{\partial t} \right]_{\text{dissipation}} = -\frac{2}{(8\pi^3)} \int d\mathbf{k}' d\mathbf{k} ds' \langle (\mathbf{s} - \mathbf{s}') | \mathbf{k} \rangle \langle \mathbf{x} + \frac{\mathbf{s}'}{2} | \rho_{op} | \mathbf{x} - \frac{\mathbf{s}'}{2} \rangle (1 - \langle \mathbf{s} | (\mathbf{k}' - \mathbf{k}) \rangle) W(\mathbf{x}, \mathbf{k}', \mathbf{k})$$

¹¹ J. B. Krieger and G. J. Iafrate, *Phys. Rev.*, B35, 9644 (1987).

¹² See, e.g. R. Lake and S. Datta, *Phys. Rev.* B45, 6670 (1992).

¹³ P. Carruthers and F. Zachariasen, *Rev. Mod. Phys.* 55, 245 (1983).

which is the coordinate representation of equation (10).

In equation (13) the variables \mathbf{x} and \mathbf{x}' are replaced by $\mathbf{x} + \mathbf{s}/2$, and $\mathbf{x} - \mathbf{s}/2$, respectively. We have evaluated equation (13) in an approximate sense through an expansion of the term $(1 - \langle s | [k' - k] \rangle) \approx i(k' - k) \cdot s + [(k - k') \cdot s]^2 / 2 + \text{higher order terms}$. From the contribution linear in s , we obtain:

$$(14) \quad \left[\frac{\partial \langle \mathbf{x} + \frac{\mathbf{s}}{2} | \rho_{op} | \mathbf{x} - \frac{\mathbf{s}}{2} \rangle}{\partial \mathbf{s}} \right]_{\text{dissipation}} \approx \frac{2i}{(8\pi^3)} \int d\mathbf{k}' d\mathbf{k} ds' \langle (s - s') | \mathbf{k} \rangle \langle \mathbf{x} + \frac{\mathbf{s}'}{2} | \rho_{op} | \mathbf{x} - \frac{\mathbf{s}'}{2} \rangle (s \cdot (k' - k)) W(\mathbf{x}; k', k)$$

Recognizing that $\frac{2}{(8\pi^3)} \int d\mathbf{k}' (k' - k) W(\mathbf{x}; k', k) = -k\Gamma(\mathbf{x}, |\mathbf{k}|)$, equation (14)

becomes;

$$(15) \quad \left[\frac{\partial \langle \mathbf{x} + \frac{\mathbf{s}}{2} | \rho_{op} | \mathbf{x} - \frac{\mathbf{s}}{2} \rangle}{\partial \mathbf{s}} \right]_{\text{dissipation}} \approx -is \cdot \int d\mathbf{k} ds' \langle (s - s') | \mathbf{k} \rangle \langle \mathbf{x} + \frac{\mathbf{s}'}{2} | \rho_{op} | \mathbf{x} - \frac{\mathbf{s}'}{2} \rangle k\Gamma(\mathbf{x}, |\mathbf{k}|)$$

Direct manipulation of equation (15) results in:

$$(16) \quad \left[\frac{\partial \langle \mathbf{x} + \frac{\mathbf{s}}{2} | \rho_{op} | \mathbf{x} - \frac{\mathbf{s}}{2} \rangle}{\partial \mathbf{s}} \right]_{\text{dissipation}} \approx -s \cdot \nabla_s \int d\mathbf{k} ds' \langle (s - s') | \mathbf{k} \rangle \langle \mathbf{x} + \frac{\mathbf{s}'}{2} | \rho_{op} | \mathbf{x} - \frac{\mathbf{s}'}{2} \rangle \Gamma(\mathbf{x}, |\mathbf{k}|)$$

For the case when the scattering is treated as independent of the magnitude of momentum, equation (16) becomes:

$$(17) \quad \left[\frac{\partial \langle \mathbf{x} + \frac{\mathbf{s}}{2} | \rho_{op} | \mathbf{x} - \frac{\mathbf{s}}{2} \rangle}{\partial t} \right]_{\text{dissipation}} \approx - \frac{\mathbf{s} \cdot \nabla_{\mathbf{x}} \langle \mathbf{x} + \frac{\mathbf{s}}{2} | \rho_{op} | \mathbf{x} - \frac{\mathbf{s}}{2} \rangle}{\tau(\mathbf{x})}$$

which is recognized, with suitable coordinate transformations, as the first part of the scattering term associated with equation (8). Higher order contributions are expected to lead, in an approximate, sense to the second scattering contribution to equation (8).

The incorporation of scattering, at least within the framework of equation (11), is a significant advance over simple relaxation time approximations in device simulations, although significant physics is missing, e.g., the effects of extremely short time events. *Nevertheless, the proposed program is concerned with treating scattering within the framework of equation (11) as a first important step to a numerical scattering approach in small systems, much within the framework of the work of Buot and Jensen¹⁴.*

In anticipation of the results of the proposed study we asked: How are the effects of scattering manifested within the framework of the density matrix in the coordinate representation? To answer this question we represented scattering, as in the below equation (18), and then related the terms of equation (18) to the approximations of the above discussion.

4.2 Phenomenological Scattering Potentials and Quasi-Fermi Levels

The calculations of figure (4) were performed within the framework of phenomenological *scattering potentials*. These contributions were expressed as:

$$(18) \quad V_{\text{scattering}}(\mathbf{x}, \mathbf{x}', t) = [E_F(\mathbf{x}, t) - E_F(\mathbf{x}', t)] + i[W(\mathbf{x}, t) + W(\mathbf{x}', t)]$$

and replaced the second line in equation (8). In equation (18) E_F and W are both real functions. In the calculations of figure 5 we restricted ourselves to one dimensional transport and conservation of momentum in a direction normal to the

¹⁴F. A. Buot and K. L. Jensen, *Phys. Rev. B*42, 9429 (1990).

propagation direction. Presently, the contributions of $E_F(x)$ have been implemented; the contributions from $W(x,t)$ are currently being implemented. In the present study:

$$(19) \quad E_F(x) - E_F(x') = \int_x^{x'} dx'' \frac{mv(x'')}{\tau(x'')}$$

where $v(x)$ is the expectation value of velocity. $v(x)$ is obtained from the velocity flux density, which is the diagonal component of the matrix:

$$(20) \quad j(x, x') = \left(\frac{\hbar}{2mi} \right) \left(\frac{\partial}{\partial x} - \frac{\partial}{\partial x'} \right) \rho(x, x')$$

Writing $j(x, x') \equiv v(x, x')\rho(x, x')$, the expectation value of velocity is: $v(x) = v(x, x)$.

As a check on our procedures it is straightforward to relate the above contributions to the first part of the Fokker-Planck dissipation. We introduce the approximation:

$$(21) \quad j(x, x') \approx [v(x, x) + (x - x') \left(\frac{\partial}{\partial x} - \frac{\partial}{\partial x'} \right) v(x, x')] \rho(x, x')$$

For sufficiently small values of $(x - x')$, $j(x, x') \approx v(x)\rho(x, x')$, and from equation (19):

$$(22) \quad E_F(x) - E_F(x') \approx \left(\frac{mv(x)(x - x')}{\tau(x)} \right).$$

Thus:

$$(23) \quad E_F(x) - E_F(x') \rho(x, x') \approx \left(\frac{\hbar}{2i\tau} \right) (x - x') \left(\frac{\partial}{\partial x} - \frac{\partial}{\partial x'} \right) \rho(x, x')$$

which has the structure of the first contribution of the second line to equation (8).

To the extent that the approximations of equations (21) and (23) are valid, the relevant equation of interest is:

$$(24) \quad \frac{\partial \rho}{\partial t} + \left(\frac{\hbar}{2mi} \right) \left(\frac{\partial^2}{\partial x^2} - \frac{\partial^2}{\partial x'^2} \right) \rho - \left(\frac{1}{i\hbar} \right) [\{ V(x,t) - V(x',t) \} - \{ E_F(x,t) - E_F(x',t) \}] \rho = 0$$

which under time independent conditions reduces to:

$$(25) \quad - \left(\frac{\hbar^2}{2m} \right) \left(\frac{\partial^2}{\partial x^2} - \frac{\partial^2}{\partial x'^2} \right) \rho + [\{ V(x,t) - V(x',t) \} - \{ E_F(x) - E_F(x') \}] \rho = 0$$

Equation (24) was implemented for the calculations of figure (5). On the basis of the last bracketed term it is clear that scattering can alter the net potential seen by the carriers, the consequent quantum distribution function and the carrier distribution.

4.3 Consistency with the Quantum Hydrodynamic Equations

While all calculations are through solutions to the quantum Liouville equation, for guidance we imposed the requirement that the results of the calculations be consistent with the broad requirements of dissipation as expressed in the infinite hierarchy of moment equations. For example, the current ($I = -ej$) was obtained subject to the condition that the energy applied to the structure was dissipated within the structure¹⁵. This condition is manifest as:

$$(26) \quad j = \left(\frac{\tau}{2mL} \right) \int_{-L}^L dx \rho(x) \frac{dV}{dx}$$

where $\rho(x) = \rho(x, x)$. Equation (18), subject to the condition of equation (20) was found to yield satisfactory results for modest values of applied bias, in that the

¹⁵ It is noted that with an energy dependent scattering mechanism this condition is often satisfied without additional constraints, providing the structure is long enough.

calculated density within the cladding regions was equal to the background density of the cladding regions, and the quasi-Fermi levels decreased monotonically within the structure, with the difference being equal to the difference in the applied potential energy. Note: for uniform fields the calculations replicate Ohm's law!

5. GENERALIZED SCHOTTKY BARRIERS FOR CV STUDIES

5.1 Introduction

In performing the CV calculations of the preceeding sections (through section 3), we have invoked the traditional means of *simulating* the effects of Schottky contacts; namely it was treated as a boundary condition. While this yields satisfactory results for structures with micron length feature sizes¹⁶, for structures with depletion zones that are sizeable fractions of the total device, the boundary condition approach is not satisfactory. Rather simulation tools must be implemented that are capable of treating the relevant quantum transport physics. The significance of dealing with the density matrix is that it is quantum mechanical, contains statistics through boundary conditions, and is thereby able to treat interfacial phenomena. The discussion below is specifically concerned with transport across a metallurgical discontinuity. *The metal Schottky semiconductor problem is treated as a heterostructure discontinuity.*

5.2 The Schottky Barrier Model

The initial stages of the model involve only single species of carriers, in the case below, electrons, and the model we chose to simulate is a standard textbook model¹⁷. The metal is taken simply as a structure with a high density of electrons; the semiconductor contains a lower density of electrons. For Ohmic

¹⁶ See, e.g. Section C of H. L. Grubin, D. K., G. J. Iafrate and J. R. Barker, *The Numerical Physics of Micron-Length and Submicron Length Semiconductor Devices*, in *VLSI Electronics, Microstructure Science*, N. Einspruch, ed Academic Press, NY (1982).

¹⁷ See, e.g. E. H. Rhoderick, *Metal-Semiconductor Contacts*, Clarendon Press, Oxford (1980) and H. K. Henisch, *Semiconductor Contacts* Clarendon Press, Oxford (1984).

metal/semiconductor (m/s) boundaries most simulation treatments represent the interface as an N^+N structure in which electrons from the heavily doped region diffuse into the lightly doped region. There is a corresponding low value of electric field at the (m/s) boundary. Zeroth order physics of the Schottky (m/s) boundary is based upon differences in the amount of energy required to remove an electron from the Fermi level in the metal to the vacuum, and from the Fermi level in the semiconductor. The transport of electrons between the semiconductor and the metal is dominated by these work functions, but is modified by the presence of interfacial states at the interface. In the discussion below rather than deal with the issues of workfunction differences, we represent the metallurgical junction as a barrier where the barrier height is taken as a measure of the workfunction difference of the two materials. The actual barrier height for any structure is determined by trial and error. In terms of the equation of motion of the density matrix this barrier appears as a contribution to the potential energy $V(x) = V_{\text{barrier}}(x) + V_{\text{self-consistent}}(x)$, where the self-consistent part arises from Poisson's equation. $V_{\text{barrier}}(x)$ is represented in figure 6.

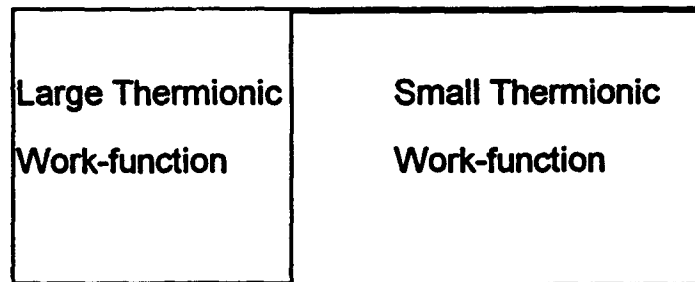


Figure 6. Schematic representation of the barrier between the metal and semiconductor, as used in the study.

While the details of the results are mitigated by the approximations necessary (at this point to get solutions) the follow picture emerges:

- The absence of a barrier at the (m/s) interface results in diffusion of charge across the boundary. There is a local depletion of charge on the 'metal' side and a local accumulation of charge on the semiconductor side.
- Introducing the barrier results in two competing effects: (i) Electrons from the semiconductor undergo real space transfer to the 'metal' resulting in a local depletion of carriers from the semiconductor and a local accumulation of

electrons in the 'metal'. (ii) The barrier reduces the amount of charge diffusing from the 'metal' to the semiconductor. The net effect of both contributions is *band bending at the interface on both the 'metal' and semiconductor side*.

- Since the height of the barrier determines the amount of charge from the heavily doped region to the semiconductor, there is likely to be a threshold to the barrier height beyond which the depletion characteristics are determined mainly by the amount of charge undergoing real space transfer on the metal.

An approximate representation of the above picture is presented below. Approximate means the model is incomplete, e.g., the model does not include holes, and there are constraints imposed by the limitations of the algorithm. First consider the approximations: (a) we assume constant effective mass.¹⁸. For a material such as GaAs in which the doping level are respectively $10^{25}/\text{m}^3$ and $10^{23}/\text{m}^3$, the Fermi energies are respectively 250.4 meV and -35.89 meV. For a built in potential of 286.3 meV. We note that if the effective mass for the high density region was that of the rest mass the built in potential would be considerably smaller. Thus before any depletion is likely to occur on the low doped side of the structure we would need to imposed a barrier of at least 240 meV. These features are illustrated in figures 7 and 8.

Figure 7 displays the electron density distribution for a zero barrier (corresponding to an N^+N^- region) and the distribution for a barrier of 200 meV. As can be seen the primary effect of the small barrier is to significantly reduce the diffusion of carriers into the lower doped region built in potential for this structure is shown in figure 2.

Figure 8 continues figure 7 but for higher values of the barrier between the 'metal' and the semiconductor. At 400 meV there is some depletion at the interface, whereas at 600 meV considerable depletion occurs on the semiconductor side of the structure. Note the presence of charge accumulation on the 'metal' side. Now the densities we have chosen to represent the metal are clearly too small

¹⁸ Calculations with a variable effective mass have been performed , but for a different set of boundary conditions. These calculations show among other things that a decrease in effective mass results in an increase in local charge density, all of which can be accounted for through analysis of the quantum potential. Results with these new boundary conditions and a variable effective mass will be reported in the near future.

and so these results are taken as being qualitatively representative of the m/s interface. The potential distributions associated with the variation in density seen in figures 7 and 8 are displayed in figures 9 and 10.

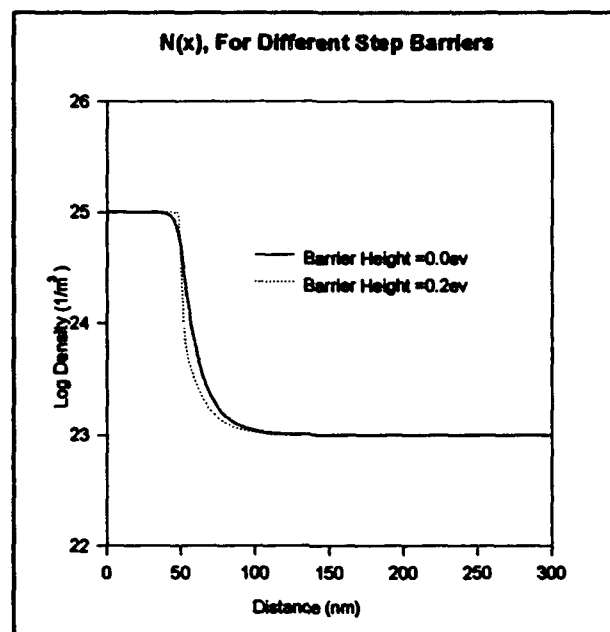


Figure 7. Density distribution as obtained from the Liouville equation for the indicated barriers.

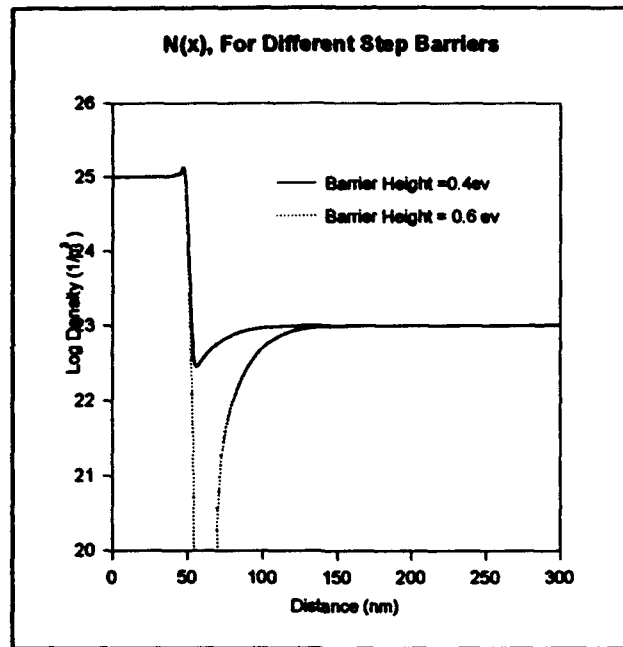


Figure 8. Density distribution as obtained from the Liouville equation for the indicated barriers.

In figure 9, we display the distribution of potential energy corresponding to figure 7. Also shown is the value of the equilibrium Fermi energy for this calculation. For both case the potential energy monotonically increases from its value on the 'metal' side to its value on the semiconductor side. The potential energy distribution in the absence of any barrier between the two regions increases according the Debye tail, while the increase in potential energy is steep when the heterostructure barrier is present.

Apart from the suppression of carrier diffusion nothing very unusual appears to be happening with regard to figure 9. The situation, as displayed in figure 10, changes when the barrier height between the 'metal' and semiconductor exceeds the built-in potential. Here the increased barrier:

- Reduces the amount of charge diffusing from the high concentration portion of the 'metal';
- Introduces real space transfer from the semiconductor to the metal¹⁹.

¹⁹ The real space transfer from the barrier region to the adjacent region, will of itself result in local charge depletion on the barrier side, with local charge accumulation on the metal side. If

- There is the presence of band bending associated with the metal²⁰.

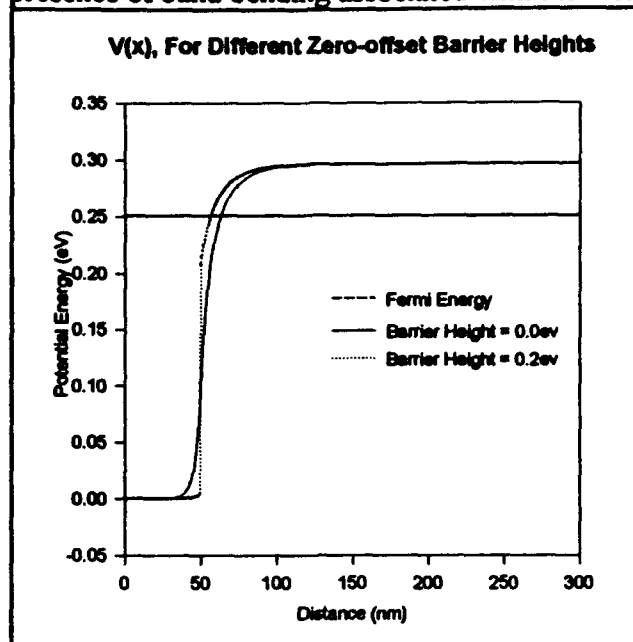


Figure 9. The self-consistent potential distribution corresponding for a zero barrier height structure and one in which the barrier height is 200 meV..

the barrier height is small enough carriers will flow from the metal to the semiconductor and essentially eliminate this charge depletion. In order for there to be any depletion on the semiconductor side the barrier must be sufficiently high.

²⁰ The band bending associated with the metal is discussed by Henisch who refers to the early work of C. A. Mead, E. H. Snow, and B. E. Deal. *Appl. Phys. Letts.* 9, 53, (1966)

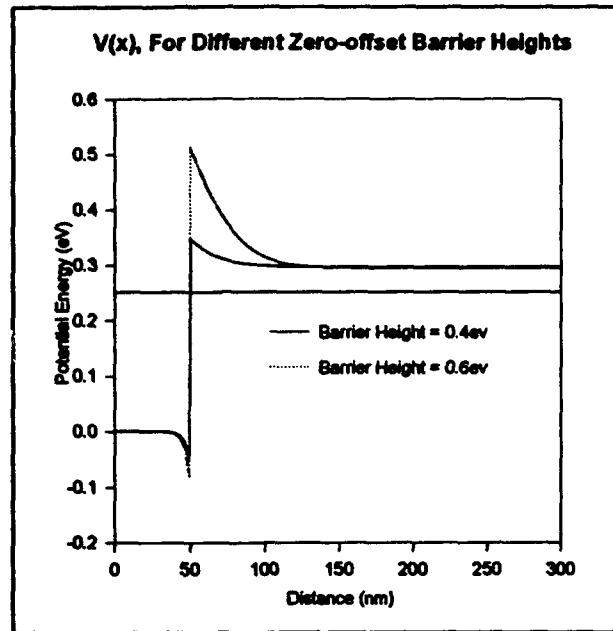


Figure 10. The self-consistent potential distribution corresponding for a 400 barrier height structure and one in which the barrier height is 600 meV.

5.3 The Schottky Barrier as an Interface Model / Quasi Fermi Levels

Within the context of this model, boundary conditions are introduced to assure that the density of the carriers on the metal side as well as at the end of the semiconductor side are constant and equal to the specified background values. This implies the presence of nonzero quasi-Fermi level distributions and represents a significant departure from the discussion of sections 2 and 3. The departure is a consequence of treating the Schottky barrier as a boundary condition, rather than as an interface problem.

What types of quasi-Fermi level distributions are we considering. If we turn to a review by Henish²¹ we see that if the classical diode theory is invoked then the quasi-Fermi levels within both the metal and semiconductor are flat and that there is an abrupt discontinuity at the metal semiconductor interface. Comments by Henish suggest that this quasi-Fermi level variation is more gradual. Figures 9

²¹ H. K. Henish, *Semiconductor Contacts*, Clarendon Press, Oxford (1984), especially section 2.2.6

and 10 represent equilibrium solutions and the quasi-Fermi level is constant. Under bias, the quasi-Fermi energy model discussed earlier (see equation 19) is imposed. To achieve the result of two essential different quasi-Fermi levels, the scattering time appearing in the above equation was increased by two orders of magnitude in the lower doped portion of the structure. While time did not permit the evaluation of the capacitance as a function of voltage under finite current conditions, we were able to obtain charge, potential energy and quasi-Fermi energy distributions for the idealized model discussed above. These are shown in the figures below.

Figure 11 is a display of the potential energy as a function of distance for different values of applied bias. Note that the bias is applied to the cathode boundary. Here the quasi-Fermi level of the metal moves with the applied bias on the metal. Then with the metal positive with respect to the semiconductor, *but with the quasi Fermi levels relative to the bottom of the conduction band remaining constant within each portion of the structure*, we get an increase in voltage at the boundary between the heavily doped region and the semiconductor.

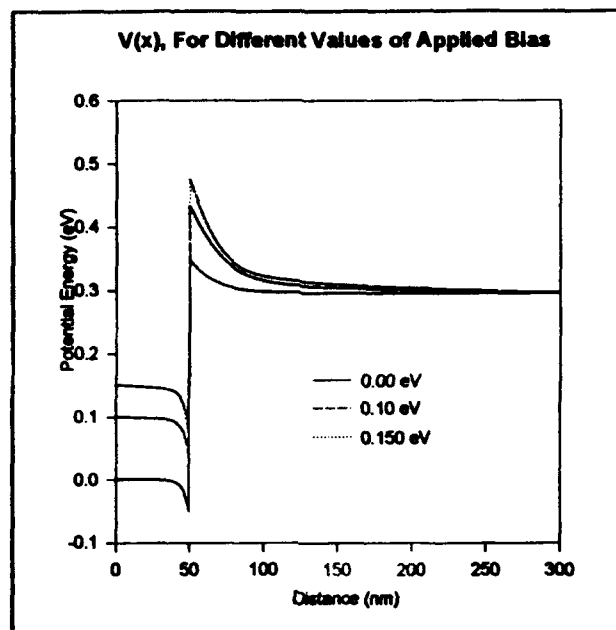


Figure 11. Potential energy distribution as a function of bias for the Schottky barrier configuration within a quasi-Fermi energy framework.

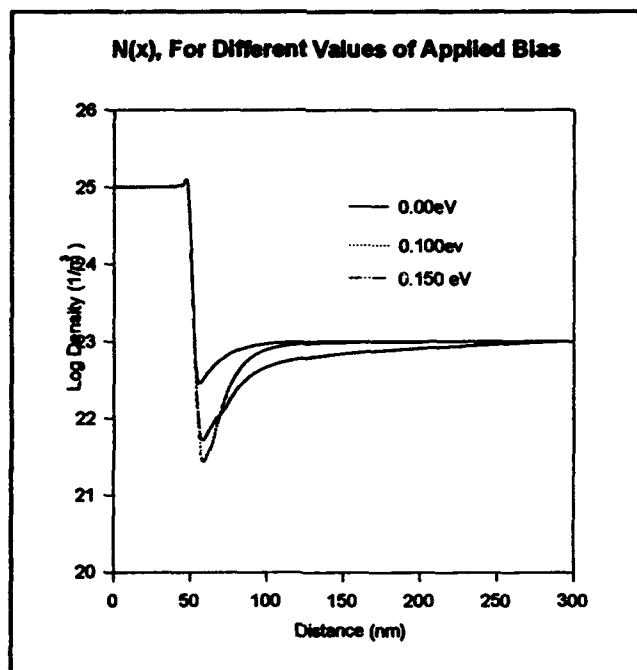


Figure 12. Density distribution as a function of bias for the Schottky barrier configuration within a quasi-Fermi energy framework.

The Schottky barrier, which is treated as an interface problem is seen to possess the same qualitative features we generally associate with the Schottky barrier as a boundary condition. Note that there is a small slope to the potential in the 'metal' portion of the structure, signifying current flow.

The density distribution corresponding to figure 11 is displayed in figure 12. We note the broad increase in the depletion zone as the bias is increased, although the minimum density for the 0.15 ev calculation is above that of the 0.10ev calculation. The details of this difference can all be found in the distribution of the Fermi energy, and indicates a dependence of the details of depletion on dissipation mechanism.

The studies illustrated in the section provide a good indication as to the means with which CV calculations should be performed. *First*, the Schottky barrier should be treated as an interface problem. Thus dissipation must be included in the model. *Second*, while we have incorporated surface states in other aspects of the Schottky as an interface problem, work must be begun to determine the effects of the interface on the CV calculations. Work with CV studies on surface states at dissimilar materials has been reported in the past. *Third*, the present program indicates that CV calculations can be performed as a function of bias when leakage current is flowing, these aspects should be included in future studies.

6. SUMMARY

The focus of the present study was the application of the quantum Liouville equation in the coordinate representation to determine the efficacy of CV measurements in determining the relevant characteristics of the nanostructure devices. While the scope of the study was limited, it appears that we can confidently use CV measurements to delineate the regions occupied by the quantum structure. The relative barrier heights of multiple heterostructures can be obtained providing the flat band conditions associated with each heteroregion are met. Details of narrow 5-10 nanometer structures cannot be obtained. There is considerable asymmetry in the charge distribution as reconstructed from the CV algorithm for symmetric structures. But as suggested by others dual polarity measurements should reveal the asymmetry as a consequence of the CV method rather than a feature of the structure.

The algorithms are being prepared for transfer to government and corporate research laboratories.
